



HAL
open science

Classical Polarizable Force Field to Study Dry Charged Clays and Zeolites

Stéphane Tesson, Wilfried Louisfrema, Mathieu Salanne, Anne Boutin,
Benjamin Rotenberg, Virginie Marry

► **To cite this version:**

Stéphane Tesson, Wilfried Louisfrema, Mathieu Salanne, Anne Boutin, Benjamin Rotenberg, et al..
Classical Polarizable Force Field to Study Dry Charged Clays and Zeolites. *Journal of Physical Chemistry C*, 2017, 10.1021/acs.jpcc.7b00270 . hal-01515667

HAL Id: hal-01515667

<https://hal.science/hal-01515667>

Submitted on 13 Nov 2018

HAL is a multi-disciplinary open access archive for the deposit and dissemination of scientific research documents, whether they are published or not. The documents may come from teaching and research institutions in France or abroad, or from public or private research centers.

L'archive ouverte pluridisciplinaire **HAL**, est destinée au dépôt et à la diffusion de documents scientifiques de niveau recherche, publiés ou non, émanant des établissements d'enseignement et de recherche français ou étrangers, des laboratoires publics ou privés.

Classical Polarizable Force Field to Study Dry Charged Clays and Zeolites

Stéphane Tesson,[†] Wilfried Louisfremea,^{‡,¶} Mathieu Salanne,[†] Anne Boutin,^{‡,¶}
Benjamin Rotenberg,[†] and Virginie Marry^{*,†}

[†]*Sorbonne Universités, UPMC Univ Paris 06, CNRS, Laboratoire PHENIX, Case 51, 4
Place Jussieu, F-75005 Paris, France*

[‡]

*Ecole Normale Supérieure, PSL Research University, UPMC Univ Paris 06, CNRS,
Département de Chimie, PASTEUR, 24 rue Lhomond, 75005 Paris, France*

[¶]

Sorbonne Universités, UPMC Univ Paris 06, ENS, CNRS, PASTEUR, 75005 Paris, France

E-mail: virginie.marry@upmc.fr

Phone: +33 (0)1 44 27 22 03

1
2
3
4
5
6
7
8
9
10
11
12
13
14
15
16
17
18
19
20
21
22
23
24
25
26
27
28
29
30
31
32
33
34
35
36
37
38
39
40
41
42
43
44
45
46
47
48
49
50
51
52
53
54
55
56
57
58
59
60

Abstract

We extend the classical Polarizable Ion Model (PIM) to charged clays. We focus on Na-, Ca-, Sr- and Cs-montmorillonite with two types of structures for the octahedral sheet : *trans*- and *cis-vacant*. The full set of parameters of the force field is determined by density functional theory calculations, using maximally localized Wannier functions with a force- and dipole-optimization procedure. Simulation results for our polarizable force field are compared to the state-of-the-art non-polarizable flexible force field named Clay Force Field (ClayFF), in order to assess the importance of taking polarization effects into account for the prediction of structural properties. This force field is validated by comparison with experimental data. We also demonstrate the transferability of this force field to other aluminosilicates by considering faujasite-type zeolites and comparing the cation distribution for anhydrous Na, Ca, and Sr Y (and X) faujasites predicted by the PIM model and with experimental data.

1
2
3
4
5
6
7
8
9
10
11
12
13
14
15
16
17
18
19
20
21
22
23
24
25
26
27
28
29
30
31
32
33
34
35
36
37
38
39
40
41
42
43
44
45
46
47
48
49
50
51
52
53
54
55
56
57
58
59
60

Introduction

Clay minerals and zeolites are nanoporous aluminosilicate materials extensively used due to their industrial importance in gas adsorption and separation. Clay minerals¹⁻³ are layered with a large lateral extension compared with their width (~ 1 nm). Zeolites^{4,5} consist of three-dimensional crystalline frameworks. Both are used in several areas, including health (drugs), domestic products (detergents and water softener), energy and environmental engineering (hydrocarbons cracking for fuel production, retention barrier preventing the release of toxic radioactive species or CO₂ into the biosphere), etc. These applications are made possible thanks to their high specific surface that confer them remarkable physicochemical properties, such as adsorption, retention, cationic exchange, etc. All these properties are modulated by the charge of the mineral framework, compensated by interlayer (clays) or extraframework (zeolites) counterions, and the presence of adsorbed molecules (the location of which depends on the position of compensating cations). Many experimental⁶⁻¹¹ and computational¹²⁻¹⁷ studies have been performed in order to understand their physicochemical properties. Whereas macroscopic descriptions are abundant (adsorption and exchange isotherm, macroscopic diffusion, etc.),¹⁸⁻²³ a detailed understanding at the microscopic scale may be difficult to obtain. Nevertheless, combining experimental with molecular simulations can provide insights into the local description of the cationic and molecular adsorption sites, of the environment of counterions, or of the fine structure of the clay and zeolite frameworks.

The reliability of molecular dynamics is based on the correct description of interaction between atoms. In the case of zeolites, most of the available force fields consider the framework as rigid and therefore require prior knowledge of the position of atoms and sites, obtained from experiments. As an example, some of us recently conducted a joint experimental and simulation study of the cation distribution in partially Ni-exchanged Y-faujasite. It was found that the migration of cations upon dehydration is strongly coupled with the framework deformation. This underlines the need for force fields accounting for the framework flexibility. In the case of clays, the force fields available in the literature are able to repro-

1
2
3
4
5
6
7
8
9
10
11
12
13
14
15
16
17
18
19
20
21
22
23
24
25
26
27
duce qualitatively the structural properties,^{17,24–27} the thermodynamics,^{13,28–31} the dynam-
ics,^{25,27,32–34} the hydrophilic/hydrophobic properties,²⁶ or the sorption of counterions.^{13,35,36}
Quantitative agreement with experiments remains however a challenge. Overall, force fields
tend to underestimate the interlayer distance^{37–39} (in particular for the bivalent counterions),
to overestimate the diffusion coefficient of water molecules,^{25,29,39,40} and to overestimate the
contact angle between a clay surface and a drop of water.²⁶ The force fields available in
the literature do not take into account the polarizability of molecules,^{27,41–43} which may
contribute to the organization of ions and water molecules near the mineral surface where
an electric field exists. Such effects were shown to be very important in other fields such as
biomolecular simulations.^{44–46} We have recently extended the force field based on the Po-
larizable Ion Model (PIM) to study clay minerals and demonstrated its ability to correctly
describe the microstructure of two neutral clays: pyrophyllite and talc.⁴⁷

28
29
30
31
32
33
34
35
36
37
38
39
40
41
42
43
44
45
46
47
48
49
50
51
52
53
54
55
56
57
58
59
60
In the present work, we extend the PIM to charged clay minerals. To parametrize the
PIM force field, we follow the same strategy described in our previous study,⁴⁷ which does
not require any experimental input. We focus on different charged clays of the smectite
family, namely Na-, Ca-, Sr- and Cs-montmorillonite. Then, we assess the transferability of
the PIM force field to other aluminosilicates by considering two different zeolites: MX and
MY faujasites (M = Na, Ca and Sr). The manuscript is organized as follows. Sections "Po-
larizable Ion Model" and "Parametrization of the Force Field" describe the different terms
of the polarizable force field and succinctly the parametrization procedure. Then, section
"Validation of the Force Field" introduces the microscopic structure of montmorillonites and
the force field is validated by comparison between experimental and simulated results. Fi-
nally, in Section "Transferability to Zeolites", after a brief introduction of the structure of
zeolites, we demonstrate the transferability of the PIM force field to faujasite-type zeolites
by studying the cationic distribution.

Polarizable Ion Model

In the PIM model, the potential energy is decomposed into four different terms:

$$V_{\text{total}} = V_{\text{Charge}} + V_{\text{Dispersion}} + V_{\text{Repulsion}} + V_{\text{Polarization}}. \quad (1)$$

The charge term corresponds to the Coulomb interaction (here in atomic units) between two atoms,

$$V_{\text{Charge}} = \sum_{i < j} \left(\frac{q_i q_j}{r_{ij}} \right), \quad (2)$$

where q_i and q_j are the charges of each atom and r_{ij} is the distance between them. In our case, formal charges are used: O^{2-} , OH^- , Mg^{2+} , Al^{3+} and Si^{4+} . Charge transfer within the hydroxyl group, of total charge -1, is modelled by partial charges on the corresponding atoms: $\text{O}_{\text{OH}}^{(2-\delta)-}$ and $\text{H}_{\text{OH}}^{(1-\delta)+}$.

The dispersion term in Eq. 1 is due to the instantaneous correlations of density fluctuations between the electronic clouds. It is given by:⁴⁸⁻⁵⁰

$$V_{\text{Dispersion}} = - \sum_{i < j} \left[f_6^{ij}(r_{ij}) \frac{C_6^{ij}}{(r_{ij})^6} + f_8^{ij}(r_{ij}) \frac{C_8^{ij}}{(r_{ij})^8} \right], \quad (3)$$

where C_6^{ij} and C_8^{ij} are the dipole-dipole and dipole-quadrupole dispersion coefficients. The Tang-Toennies damping function f_n^{ij} is used to correct the short-range interaction as:⁵¹

$$f_n^{ij}(r_{ij}) = 1 - e^{-b_n^{ij} r_{ij}} \sum_{k=0}^n \frac{(b_n^{ij} r_{ij})^k}{k!}, \quad (4)$$

where $\frac{1}{b_n^{ij}}$ is the range of the damping. The repulsion term in Eq. 1 is modelled using a simple decaying exponential:

$$V_{\text{Repulsion}} = \sum_{i < j} A_{ij} e^{-B_{ij} r_{ij}}, \quad (5)$$

where A_{ij} and B_{ij} are two parameters. Finally, the polarization term in Eq. 1 is composed of

3 contributions: charge-dipole and dipole-dipole interactions, as well as the energy cost for deforming the electronic cloud of the atom:

$$V_{\text{Polarization}} = \sum_{i < j} \left[\frac{q_i \mathbf{r}_{ij} \cdot \boldsymbol{\mu}_j}{r_{ij}^3} g_4^{ij}(r_{ij}) - \frac{\boldsymbol{\mu}_i \cdot \mathbf{r}_{ij} q_j}{r_{ij}^3} g_4^{ji}(r_{ij}) + \frac{\boldsymbol{\mu}_i \cdot \boldsymbol{\mu}_j}{r_{ij}^3} - \frac{3(\mathbf{r}_{ij} \cdot \boldsymbol{\mu}_i)(\mathbf{r}_{ij} \cdot \boldsymbol{\mu}_j)}{r_{ij}^5} \right] + \sum_i \frac{|\boldsymbol{\mu}_i|^2}{2\alpha^i}, \quad (6)$$

where α^i is the polarizability of ion i , $\boldsymbol{\mu}_i$ and $\boldsymbol{\mu}_j$ are the induced dipoles, g^{ij} is the short-range correction to the multipolar expansion by the Tang-Toennies damping function:

$$g_4^{ij}(r_{ij}) = 1 - c_{ij} e^{-b_D^{ij} r_{ij}} \sum_{k=0}^4 \frac{(b_D^{ij} r_{ij})^k}{k!}. \quad (7)$$

The polarization term includes many-body electrostatic effects since the induced dipoles fluctuate along the simulation depending on the positions of all the ions. They are calculated at each molecular dynamics step by minimizing the polarization energy:

$$\left(\frac{\partial V_{\text{Polarization}}}{\partial \mu_\alpha^i} \right) = 0. \quad (8)$$

The purpose of the present work is to derive all the parameters of the PIM repulsion and polarization terms for the atomic interactions between cations and clay layers. The parameters for the interactions between the atoms constituting the sheets and between the cations are taken from preliminary studies.^{47,52} We now briefly describe the procedure for obtaining the parameters from *ab initio* calculations, and refer the reader to our previous work⁴⁷ for a complete description.

Parametrization of the Force Field

Optimization Procedure

The optimization procedure aims at finding the set of parameters (A_{ij} , B_{ij} , c_{ij} and b_D^{ij}) that minimize the error made in the classical calculation of the forces and dipoles with respect to a series of reference DFT calculations. To determine A_{ij} and B_{ij} parameters for the repulsion potential (Eq. 5) and c_{ij} and b_D^{ij} parameters of the Tang-Toennies function (Eq. 7) for the polarization potential (Eq. 6), we used exactly the same process as for dry pyrophyllite and talc.⁴⁷ The optimization procedure can be summarized as follows:

1. Generation of a series of representative configurations using classical MD
2. DFT calculations on each of these configurations
 - (i) Determination of the ground-state wavefunction, which provides the DFT forces
 - (ii) Wannier localization,⁵³⁻⁵⁶ from which the DFT induced dipoles are calculated
3. Minimization of the error function on the dipoles χ_{Dipole}^2 with respect to the parameters of the polarization term ($V_{\text{Polarization}}$) and of χ_{Force}^2 with respect to the repulsion term ($V_{\text{Repulsion}}$):

$$\chi_{\text{Dipoles}}^2(b_D^{ij}, c_{ij}) = \frac{1}{N_{\text{conf}}} \frac{1}{N_{\text{atom}}} \sum_{\text{conf}} \sum_{\text{atom}} \frac{\|\boldsymbol{\mu}^{\text{classical}} - \boldsymbol{\mu}^{\text{DFT}}\|^2}{\|\boldsymbol{\mu}^{\text{DFT}}\|^2}, \quad (9)$$

$$\chi_{\text{Forces}}^2(A_{ij}, B_{ij}, b_D^{ij}, c_{ij}) = \frac{1}{N_{\text{conf}}} \frac{1}{N_{\text{atom}}} \sum_{\text{conf}} \sum_{\text{atom}} \frac{\|\mathbf{F}^{\text{classical}} - \mathbf{F}^{\text{DFT}}\|^2}{\|\mathbf{F}^{\text{DFT}}\|^2}, \quad (10)$$

where N_{conf} is the number of configurations on which DFT calculations are performed, N_{atom} is the number of atoms per configuration, $\boldsymbol{\mu}^{\text{classical}}$ are the dipoles obtained by classical molecular dynamics using a given set of parameters. $\mathbf{F}^{\text{classical}}$ are the forces obtained by classical molecular dynamics.

In this work, we determine the parameters of the repulsion potential (Eq. 5) and of the Tang-Toennies function (Eq. 7) of the polarization potential (Eq. 6) for the interactions between cations and the atoms of the clay layer. All the other interactions, including dispersion terms, are taken from our previous study.⁴⁷

Simulation Details

The montmorillonite simulation boxes contain two clay layers of lateral dimensions $20.72 \times 17.96 \text{ \AA}^2$, corresponding to 8 unit cells of formula $X_{0.75/n}\text{Si}_8\text{Al}_{3.25}\text{Mg}_{0.75}\text{O}_{20}(\text{OH})_4$ per layer (where $X = \text{Na}^+$, Ca^{2+} , Sr^{2+} or Cs^+ and n is the formal charge of counterions). The interlayer spacing is fixed to 9.7 \AA , 9.5 \AA , 9.5 \AA and 10.8 \AA for Na-montmorillonite,⁵⁷ Ca-montmorillonite,⁵⁸ Sr-montmorillonite⁵⁸ and Cs-montmorillonite⁵⁷ respectively. To generate the initial trajectory (i.e. prior to the force field parameterization), the interactions between cations and basal or hydroxyl oxygen atoms are chosen empirically and taken equal to the interaction between the same cations and the oxygen atom of water from our previous work.^{52,59} The short-range cation-cation interactions are treated by the Lennard-Jones potential,⁵² but it should be noted that such short-range interactions are not crucial due to the strong electrostatic repulsion between cations. The parameters C_6^{ij} , C_8^{ij} et b_n^{ij} of the cation-oxygen interactions, of the dipersion potential (Eq. 3), are taken equal to the oxygen- X ⁴⁷ (where $X = \text{Al}$, Mg or Si). The bond between the hydrogen and the oxygen atoms of the hydroxyl group is rigid. During subsequent iterations of the procedure described above, new configurations used for the dipole- and force-matching are generated using PIM with the current values of these parameters. Molecular dynamics simulations are performed with the version 2.4 of the CP2K simulation package.⁶⁰ Periodic boundary conditions are used in the three directions of space. The temperature $T = 300 \text{ K}$ is controlled via a Martyna *et al.* thermostat⁶¹ with a time constant equal to 1 ps. Electrostatic interactions are computed using dipolar Ewald summation,^{62,63} with a tolerance of 10^{-7} . For each system, we perform an equilibration of 50 ps followed by a 50 ps production run, using a time step of 0.5 fs.

From the classical MD trajectories we sample equilibrium configurations which should be sufficiently separated in order to be independent from each other. The parametrization of the force field is achieved using $N_{\text{conf}} = 6$ representative configurations per montmorillonite (3 *tv*-Na-montmorillonite and 3 *cv*-Na-montmorillonite, see below for their descriptions). We have tried to use more configurations when adjusting the parameters, and we observed that it did not influence further the value of the parameters. Density Functional Theory (DFT) calculations are performed on these configurations with the PBE⁶⁴ functional for all the systems. Goedecker-Teter-Hutter⁶⁵⁻⁶⁷ pseudopotentials are used with the DZVP plane-wave basis sets⁶⁸ and an energy cutoff of at least 400 Ry. After determining the ground-state wavefunctions, the forces acting on each atom are computed and the dipoles are calculated from the Maximally Localized Wannier Functions^{67,69,70} (MLWFs). All these calculations are performed with the CP2K simulation package.⁶⁰ The numerical minimization of forces and dipoles are performed with the Minuit library.⁷¹

Force Field Parameters

Figures 1 and 2 illustrate the comparison between the dipoles and the forces for one of the montmorillonite configurations calculated with the classical force field and from the DFT calculations. The corresponding error functions, χ_{Dipoles}^2 and χ_{Forces}^2 are shown in Table 1.

Table 1: χ^2 for the dipoles and the forces for charged clays

Systems	χ_{Dipoles}^2	χ_{Forces}^2
Na-montmorillonite	0.229	0.787
Ca-montmorillonite	0.073	0.815
Sr-montmorillonite	0.061	0.790
Cs-montmorillonite	0.076	0.887

Most of the errors on the forces come from the forces exerted on the aluminum, silicon,

1
2
3
4 magnesium and apical oxygen atoms. All errors observed on the dipoles come from the
5 oxygen atoms of the hydroxyl groups. χ_{Dipoles}^2 and χ_{Forces}^2 obtained for the charged clays are
6 larger than those for the neutral pyrophyllite clay (0.029 and 0.25, respectively⁴⁷). Most of
7 these relative errors are due to very small values of forces and dipoles. As we will see later,
8 the resulting force field is however able to capture the structural feature of the studied clays.
9
10 All the parameters are summarized in Tables 2, 3 and 4. The parameters of atoms layer are
11 reported in the supporting information.⁴⁷ The relevance of including polarization into the
12 force field to capture many-body effects can be demonstrated by considering the dipoles of
13 different oxygen types in the mineral structure. Specifically, we show in the Supplementary
14 Figure S1 that the dipoles of apical and surface oxygen atoms are very different. Therefore,
15 including the polarizability of these atoms in the force field allows a transferable description
16 of both types of oxygen atoms with the same set of parameters. In a non-polarizable model,
17 these different types of oxygen atoms would typically require different set of parameters.
18 Moreover, we note that, even in that case, such a description would not allow capturing the
19 change in the charge distribution around surface atoms in the presence of cations, which
20 can be significant in particular with multivalent ions and influences their adsorption at the
21 surface.
22
23
24
25
26
27
28
29
30
31
32
33
34
35
36
37
38
39

40 Validation of the Force Field

41 Structure of Montmorillonites

42
43
44 Montmorillonite is a charged clay belonging to the same family as pyrophyllite, namely dioc-
45 tahedral clays. They are composed of layers piled on top of each other to form particles. Each
46 layer consists of two tetrahedral sheets sandwiching an octahedral sheet (TOT structure).
47 In neutral pyrophyllite, these sheets are thus made from two crystallographic units: SiO_4
48 tetrahedra and $\text{AlO}_4(\text{OH})_2$ octahedra, represented in Figure 3a and b. Tetrahedral sheets
49 are composed of basal oxygen (O_b), apical oxygen (O_a) and silicium (Si) atoms. The octa-
50
51
52
53
54
55
56
57
58
59
60

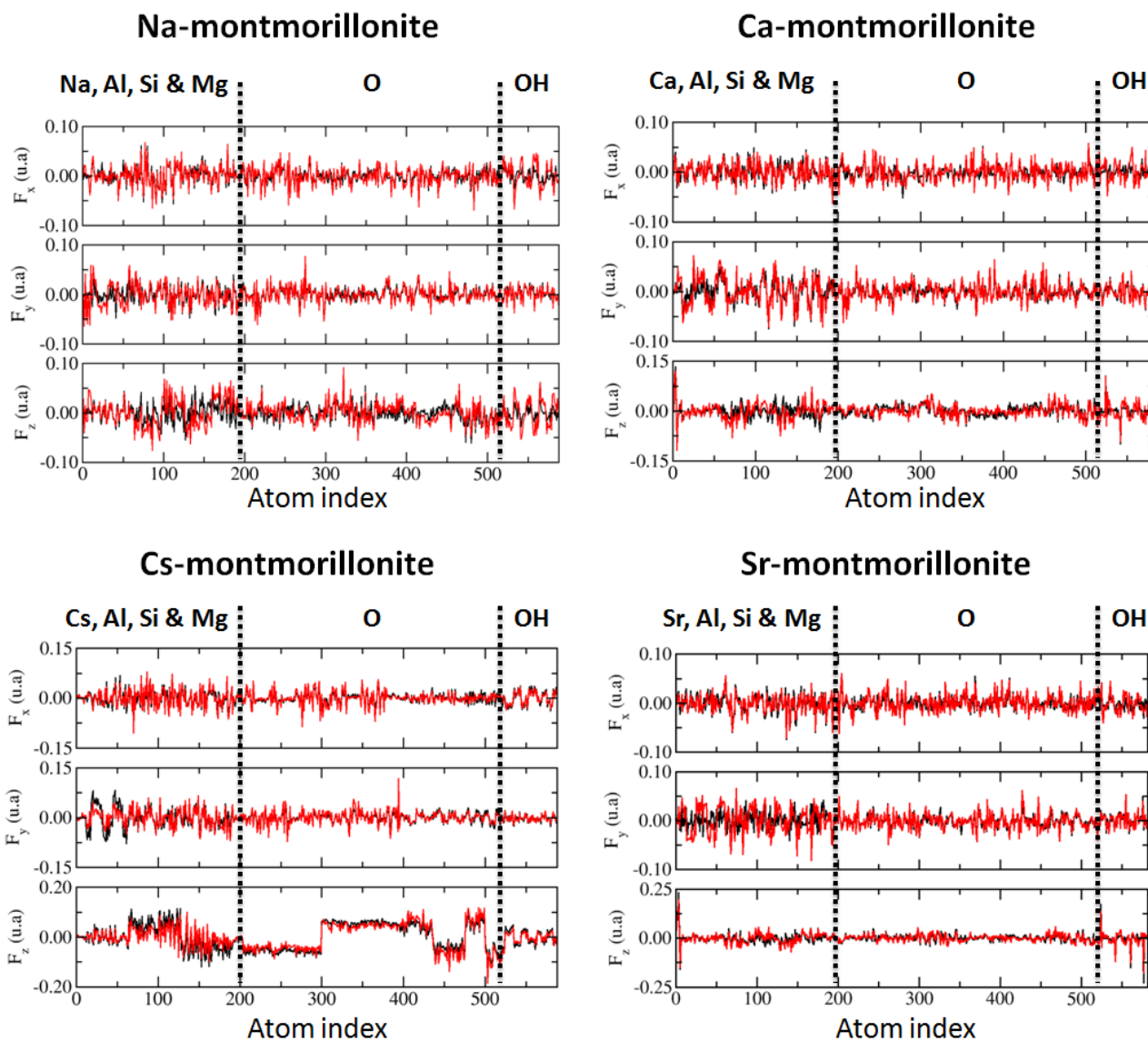


Figure 1: Forces for each atom for one of the montmorillonite configurations. The predictions of the classical force field (black lines) for the force components (F_x , F_y and F_z) are compared to the DFT results (red lines).

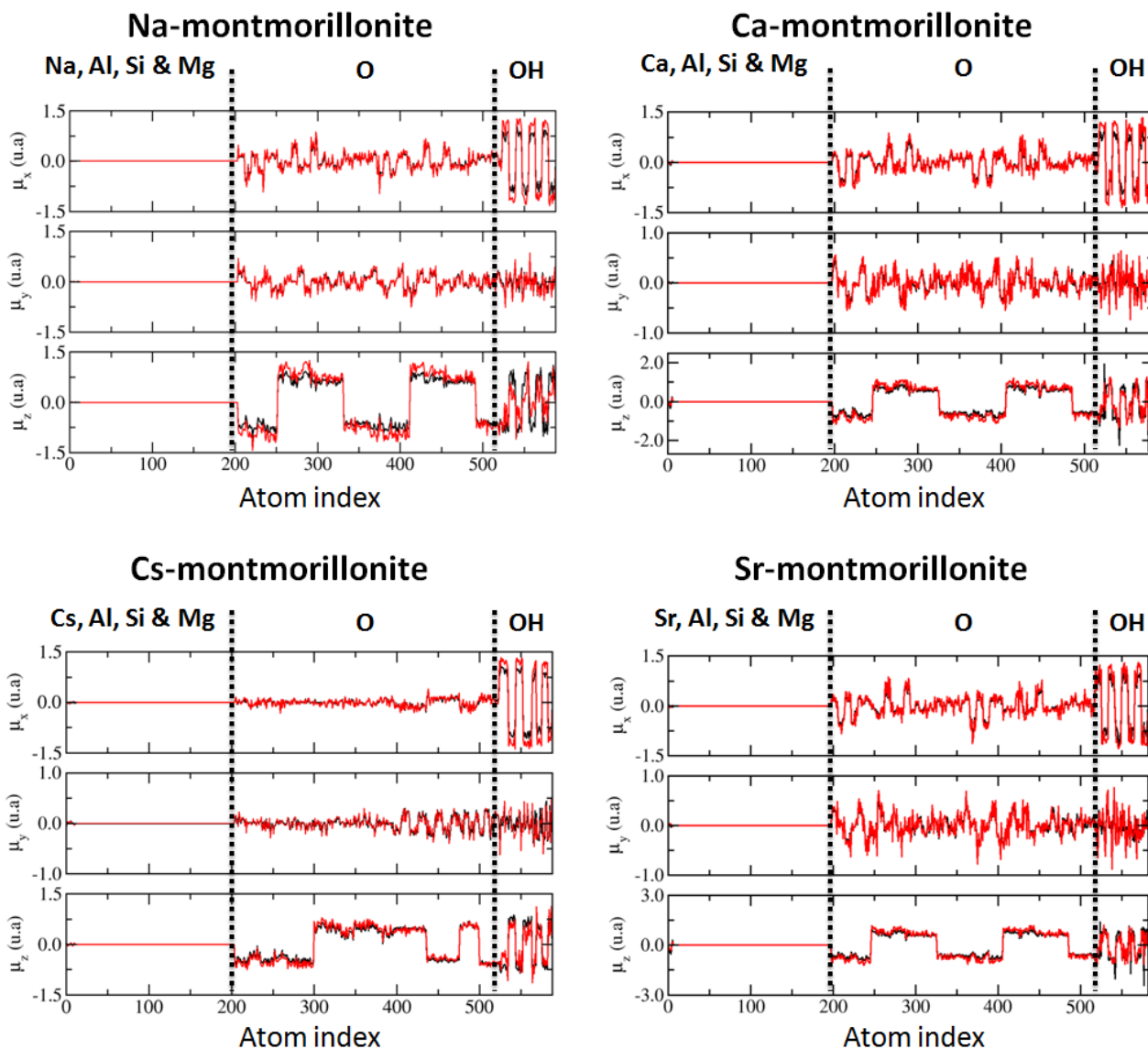


Figure 2: Dipoles for each atom for one of the montmorillonite configurations. The predictions of the classical force field (black lines) for the dipole components (μ_x , μ_y and μ_z) are compared to the DFT results (red lines).

Table 2: Parameters of the PIM force field for the repulsion and polarization terms for the interactions between the cations and the oxygen atoms from the sheet. δ is the transferred charge ($\delta = + 0.8983$).

Ion pair (ij)	A_{ij} (Ha)	B_{ij} (\AA^{-1})	C_6^{ij} (Ha. \AA^6)	C_8^{ij} (Ha. \AA^8)	b_n^{ij} (\AA^{-1})	Damping interaction between q_i and μ_j	
						b_D^{ij} (\AA^{-1})	c_{ij} (-)
$O^{2-}-Na^+$	30.002	3.300	0.048	0.156	4.168	4.330	2.133
$O^{2-}-Ca^{2+}$	20.004	2.543	0.048	0.156	4.168	5.999	0.028
$O^{2-}-Sr^{2+}$	20.064	2.520	0.048	0.156	4.168	5.769	2.178
$O^{2-}-Cs^+$	20.001	2.748	0.048	0.156	4.168	5.943	0.219
$O_{OH}^{(2-\delta)-}-Na^+$	4019.112	5.998	0.048	0.156	4.168	5.678	3.468
$O_{OH}^{(2-\delta)-}-Ca^{2+}$	4998.674	5.654	0.048	0.156	4.168	5.999	0.001
$O_{OH}^{(2-\delta)-}-Sr^{2+}$	4994.966	5.419	0.048	0.156	4.168	5.992	0.001
$O_{OH}^{(2-\delta)-}-Cs^+$	4000.000	5.100	0.048	0.156	4.168	5.686	0.006

Table 3: Polarization damping parameters of the PIM force field. δ is the transferred charge ($\delta = + 0.8983$).

Charge Ion (i)	Dipole Ion (j)	b_D^{ij} (\AA^{-1})	c_{ij} (-)
Na ⁺	Al ³⁺	3.702	3.344
	Si ⁴⁺	3.663	3.774
	Mg ²⁺	2.150	0.013
	O ²⁻	3.648	1.762
	O _{OH} ^{(2-δ)-}	3.009	4.870
	H _{OH} ^{(1-δ)+}	2.716	3.916
Ca ²⁺	Al ³⁺	2.956	4.919
	Si ⁴⁺	5.399	2.581
	Mg ²⁺	5.774	3.652
	O ²⁻	5.479	4.770
	O _{OH} ^{(2-δ)-}	4.153	4.983
	H _{OH} ^{(1-δ)+}	3.630	4.996
Sr ²⁺	Al ³⁺	2.765	4.999
	Si ⁴⁺	4.504	4.789
	Mg ²⁺	5.669	4.516
	O ²⁻	4.461	2.112
	O _{OH} ^{(2-δ)-}	2.957	1.828
	H _{OH} ^{(1-δ)+}	2.058	4.994
Cs ⁺	Al ³⁺	2.001	0.932
	Si ⁴⁺	3.383	3.609
	Mg ²⁺	2.007	3.901
	O ²⁻	2.865	0.599
	O _{OH} ^{(2-δ)-}	2.449	4.945
	H _{OH} ^{(1-δ)+}	5.872	2.404

Table 4: Atomic polarizabilities.

Ions	O^{2-}	O_{OH}^-	Na^+	Ca^{2+}	Sr^{2+}	Cs^+
α^i (\AA^3)	0.91	2.39	0.18	0.44	0.81	2.02

hedral sheet contains apical oxygen and aluminium (Al) atoms, as well as hydroxyl groups (OH). In montmorillonite, some octahedral Al are replaced by magnesium (Mg), resulting in a negative charge of the sheet compensated by counterions located in the interlayer space (here Na^+ , Ca^{2+} , Sr^{2+} or Cs^+).

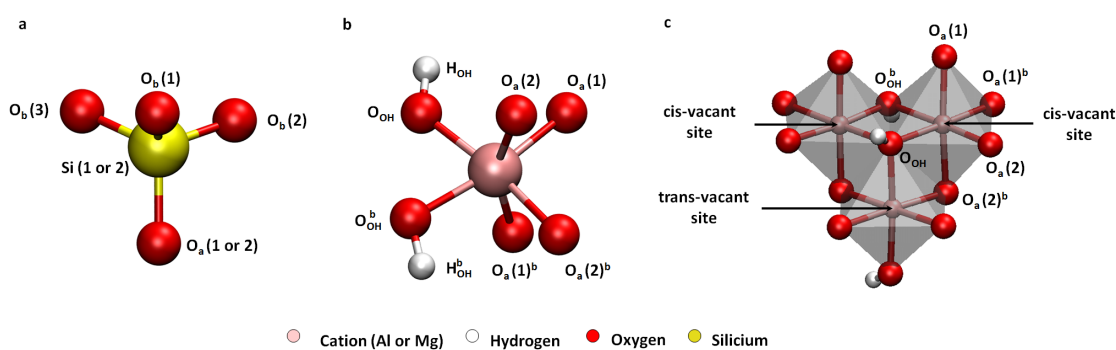


Figure 3: Nomenclature of the atoms. a) tetrahedron, b) octahedron and c) *tv*- and *cv*-sites (trans- and cis-vacant respectively).

Each tetrahedron is linked to adjacent tetrahedra by basal oxygen atoms (O_b) to form an infinite hexagonal basal plane (Figure 4a). The tetrahedral and octahedral sheets are connected by the apical oxygen (O_a). Within the octahedral sheet, each octahedron shares two hydroxyl oxygens (O_{OH}) and four apical oxygens (O_a). An octahedral site can be occupied by a six-fold coordinated cation. In montmorillonite, a dioctahedral clay type, two thirds of these sites are occupied by trivalent ions Al^{3+} or divalent ions Mg^{2+} , as illustrated in Figures 4b and 4c. Depending on the location of the vacancy there are two types of octahedral sheets:⁷² i) the two octahedra occupied by Al^{3+} cations share an edge with two hydroxyl groups, *i.e.* occupy so called cis sites, and the remaining trans site is vacant – such an octahedral sheet is thus called *trans-vacant* (*tv*-, illustrated in Figures 3c and 4b); ii)

the two octahedra occupied by Al^{3+} cations share an edge with one hydroxyl group and one apical oxygen, *i.e.* occupy one cis and one trans sites, so that one cis site remains vacant – such an octahedral sheet is called *cis-vacant* (*cv-*, illustrated in Figures 3c and 4c). Vantelon *et al*⁷³ have shown that substitution occurred predominantly in cis sites for a Wyoming-type montmorillonite. This clay is the one that we have used for our *cv*-montmorillonite systems, except that we have slightly simplified the system by substituting only the "cis" sites. For this study, we worked with *tv*-montmorillonite and *cv*-montmorillonite in order to assess the ability of the polarizable force field to differentiate them. A side view of the montmorillonite systems are given in Figure 5.

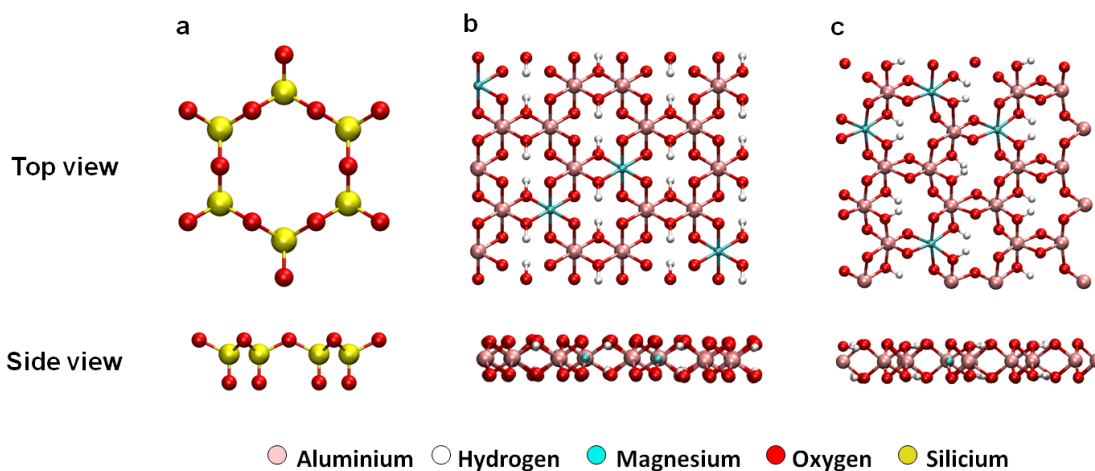


Figure 4: Top and side views of a) tetrahedral, b) *tv*-octahedral and c) *cv*-octahedral sheet.

Systems and Simulation Details

We now proceed to the validation of the force field against experimental data pertaining to the structure of montmorillonite. We consider three sizes of montmorillonite simulation cells for each *tv*- and *cv*-clay to assess the possible influence of finite-size effects. Table 5 indicates the different box lengths A, B and C. The simulation details are the same as above. The simulations are first performed in the NVT ensemble during 100 ps in order to equilibrate each system. Then, simulations are performed in the anisotropic NPT ensemble (all box

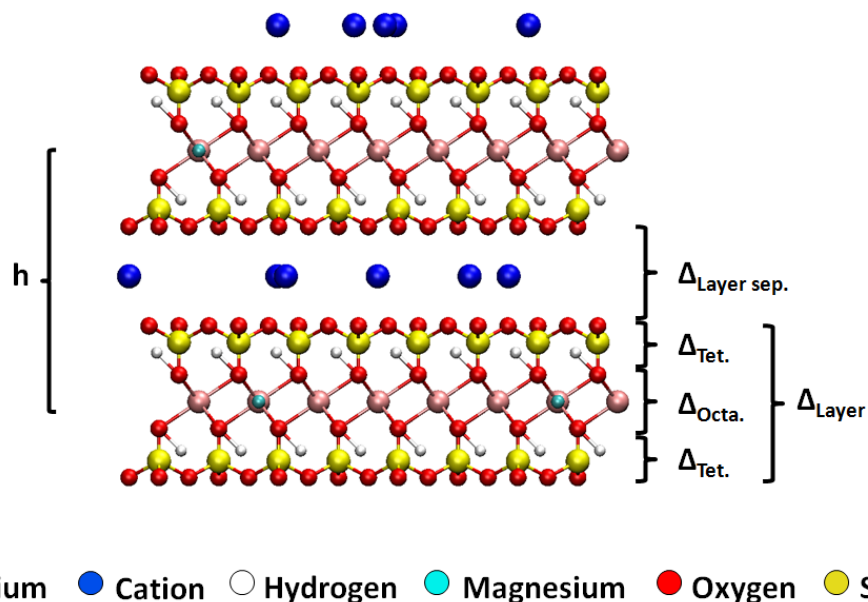


Figure 5: Side view of the ideal *tv*-montmorillonite layers. h is the average interlayer distance, $\Delta_{\text{Layer sep.}}$ is the average thickness of the layer separation, $\Delta_{\text{Tet.}}$ and $\Delta_{\text{Octa.}}$ are the average thicknesses of the tetrahedral and octahedral sheets, while Δ_{Layer} is that of the layer.

lengths and angles are allowed to evolve independently) under a pressure of 1 bar during 150 ps of equilibration followed by 150 ps of production. The pressure is controlled by an extension of the Nose-Hoover barostat developed by Martyna *et al*^{61,74} with a barostat and a thermostat time constant respectively equal to 2 ps and 1 ps. Simulations under the same conditions were performed for both our new polarizable force field and the state-of-the-art non-polarizable force field ClayFF.⁴¹ The simulations with the PIM are only around 5 times more computationally expensive than with ClayFF. Further improvements could be obtained by using approaches such as the predictor-corrector algorithm of Kolafa⁷⁵.

Lattice Parameters

The unit cell parameters obtained for the equilibrated systems are summarized in Table 6 and the lattice parameters are exposed on the Figure 6. Since the effect of system size is very limited, we report here averages over all the systems. The results obtained for the elementary unit cell parameters a , b , α , β , and γ with ClayFF or PIM, for all clays, are in good agreement

Table 5: Simulated systems for montmorillonite: A, B and C are the initial box sizes.

Systems <i>tv-</i> and <i>cv-</i>	Supercell dimensions	A (Å)	B (Å)	C (Å)	Number of atoms
	$8 \times 4 \times 2$		35.88		2608
Na-montmorillonite	$8 \times 5 \times 2$	41.28	44.85	19.40	3260
	$8 \times 6 \times 2$		53.82		3912
	$8 \times 4 \times 2$		35.88		2584
Ca-montmorillonite	$8 \times 5 \times 2$	41.28	44.85	19.00	3230
	$8 \times 6 \times 2$		53.82		3876
	$8 \times 4 \times 2$		35.88		2584
Sr-montmorillonite	$8 \times 5 \times 2$	41.28	44.85	19.00	3230
	$8 \times 6 \times 2$		53.82		3876
	$8 \times 4 \times 2$		35.88		2608
Cs-montmorillonite	$8 \times 5 \times 2$	41.28	44.85	21.60	3260
	$8 \times 6 \times 2$		53.82		3912

with the experimental data. Both force fields ensure the integrity of the elementary cell. Experimentally, the distance h ranges between 9.5–9.7 Å for Na-montmorillonite,^{57,76–80} 9.5–11.65 Å for Ca-montmorillonite,^{58,76–79} 9.5–10.0 Å for Sr-montmorillonite^{58,76,78,79} and 10.7–12.0 Å for Cs-montmorillonite.^{57,79,81} The PIM reproduces the experimental h distance more accurately than the ClayFF for most of cations, *i.e.* Na⁺, Ca²⁺ and Sr²⁺, while both for force fields predict similar values in good agreement with experiments for Cs⁺. These different values obtained with PIM and ClayFF may come from the structure of the cavities, as discussed below.

Table 6: Unit cell parameters of montmorillonite (averaged over *tv*- and *cv*-montmorillonite and over the various supercells): lattice parameters a , b , c and cell angles α , β , γ . Standard errors (SE) of 0.04 Å and 0.8 degrees, respectively, are calculated by the block averaging method.^{82,83}

Force field	Counterion	a (Å)	b (Å)	c (Å)	h (Å)	α (°)	β (°)	γ (°)
PIM	Na ⁺	5.19	9.00	9.77	9.61	89.9	98.9	90.1
	Ca ²⁺	5.21	8.97	10.08	10.00	88.8	97.2	90.2
	Sr ²⁺	5.22	9.01	10.15	10.04	90.0	98.3	90.1
	Cs ⁺	5.22	8.96	10.94	10.69	89.9	98.5	90.0
ClayFF	Na ⁺	5.20	9.00	9.54	9.41	88.5	97.2	90.0
	Ca ²⁺	5.21	9.04	9.59	9.41	90.8	98.6	89.8
	Sr ²⁺	5.20	9.04	9.82	9.59	90.8	99.0	90.1
	Cs ⁺	5.19	9.00	10.98	10.75	90.0	99.5	90.0
Exp. ⁷²	Na ⁺	5.18	8.98			90.0	99.5	90.0
Exp. ^{57,76–80}	Na ⁺				9.5–9.7			

Internal Structure of the Layers

The average bond lengths and angles obtained by both force fields for *tv*- and *cv*-montmorillonites are summarized in Supplementary Tables S2 and S3, respectively. The average thickness of

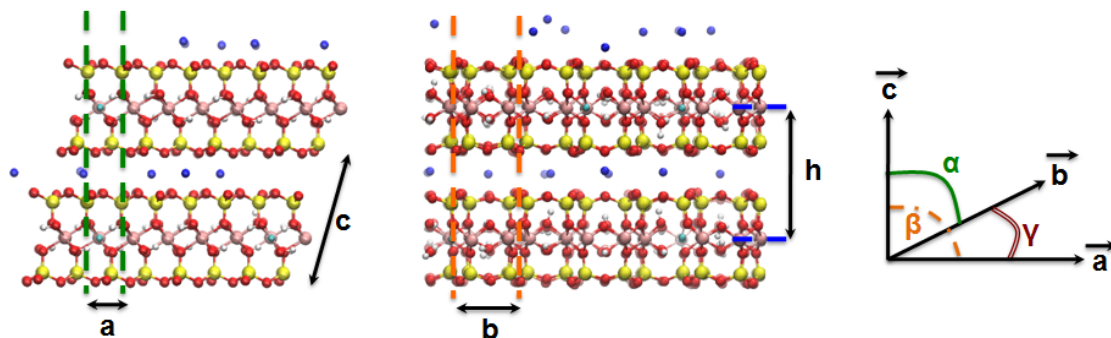


Figure 6: Lattice parameters.

the tetrahedral ($\Delta_{\text{Tet.}}$) and octahedral ($\Delta_{\text{Octa.}}$) sheets, the layer (Δ_{Layer}), the layer separation ($\Delta_{\text{Layer sep.}}$), the silicium-apical oxygen distance⁴⁷ $\Delta_{\text{Si-O}_a}$, the angles⁴⁷ α_1 , α_2 , the tilt γ_{tilt} and the rotation angle⁴⁷ of tetrahedra $\alpha_{\text{rot.}}$ obtained for the various systems are summarized in Table 7 and shown in Figure 7.

Table 7: Average thickness of the tetrahedral $\Delta_{\text{Tet.}}$ and octahedral $\Delta_{\text{Octa.}}$ sheets, layer Δ_{Layer} and layer separation $\Delta_{\text{Layer sep.}}$ (see Figure 5), silicium-apical oxygen distance $\Delta_{\text{Si-O}_a}$, angles α_1 , α_2 , tilt γ_{tilt} and rotation angle of tetrahedra $\alpha_{\text{rot.}}$. Standard errors (SE) of 0.07 Å and 1 degrees for distances and angles, respectively, are calculated by the block averaging method.^{82,83}

Force field	$\Delta_{\text{Tet.}}$	$\Delta_{\text{Octa.}}$	Δ_{Layer}	$\Delta_{\text{LayersSep.}}$	$\Delta_{\text{Si-O}_a}$	γ_{tilt}	α_1	α_2	$\alpha_{\text{rot.}}$
	(Å)	(Å)	(Å)	(Å)	(Å)	(°)	(°)	(°)	(°)
PIM	2.16	2.22	6.54	3.06	1.58	7	110	132	11
ClayFF	2.10	2.27	6.47	2.94	1.58	4	119	121	1

Octahedral Sheet

We now examine the differences between *tv*- and *cv*-montmorillonite by looking at the structure of the octahedral sheet and investigate the ability of the force fields to capture such differences. More precisely, we analyze the distance $d_{\text{O}_{\text{OH}}-\text{O}_{\text{OH}}^b}$ between the oxygens of the hydroxyl groups of the same edge of an octahedron (Figure 3). Experimentally, Wilson *et al.* have shown that $d_{\text{O}_{\text{OH}}-\text{O}_{\text{OH}}^b}$ differs in *tv*- and *cv*-montmorillonite. This difference could possibly be due to the orientation of these hydroxyl groups: towards the center of the cav-

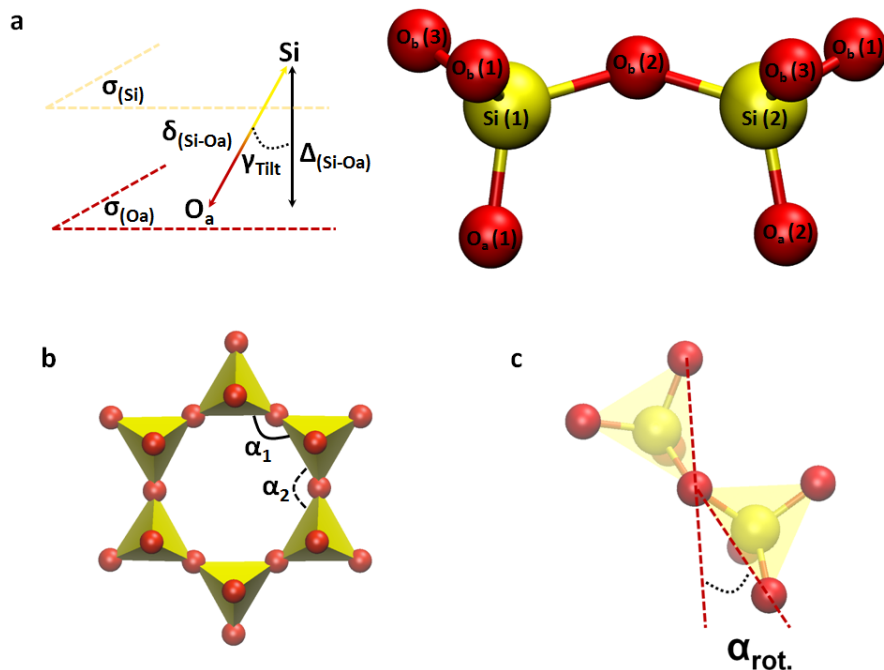


Figure 7: (a) Definition of the tilt angle of tetrahedra, (b) and (c) bottom-up view of the tetrahedral sheet ; $\alpha_1 = 120 + 2 \times \alpha_{rot}$ and $\alpha_2 = 120 - 2 \times \alpha_{rot}$

ity for *cv*-montmorillonite, in contrast to *tv*-montmorillonite (Figures 3 and 4). In order to minimize the interaction between these two hydroxyl groups, the $d_{O_{OH}-O_{OH}^b}$ distance is larger in *cv*-montmorillonite (2.85-2.88 Å) than in the *tv*-montmorillonite (2.40-2.50 Å). By simulation, the distances $d_{O_{OH}-O_{OH}^b}$ are well reproduced for both clay types with the PIM force field, with $d_{O_{OH}-O_{OH}^b} = 2.89(5)$ and $2.42(4)$ Å for *cv*- and *tv*-montmorillonite, respectively. In the case of ClayFF, the distance $d_{O_{OH}-O_{OH}^b}$ is reproduced in *cv*-montmorillonite (2.92(5) Å) whereas it is overestimated in *tv*-montmorillonite (2.85(4) Å). Thus, the PIM force field better describes the difference between *tv*- and *cv*-montmorillonite.

Tetrahedral Sheet

For both ClayFF and PIM, the average bond lengths and angles in Supplementary Tables S2 and S3 are similar to the results obtained on pyrophyllite.⁴⁷ Specifically, in contrast to ClayFF the PIM force field is able to capture the deformation of the tetrahedral sheets

1
 2
 3
 4 characterized by the following features: i) the angle $O_a-Si-O_b(2)$ is slightly wider than
 5 the two others $O_a-Si-O_b(1)$ and $O_a-Si-O_b(3)$, ii) the tetrahedral sheet adjusts its lateral
 6 dimensions, thus causing changes in structure (rotation and tilt of the tetrahedra, which
 7 modify the shape of the cavities; this important difference with ClayFF is illustrated in
 8 Figure 8) and iii) the average thickness of the tetrahedral layers ($\Delta_{Tet.}$) is comparable to
 9 that in pyrophyllite. Experimentally, on montmorillonites and clays belonging to the same
 10 family, Tsipursky *et al.*⁷² and Drits *et al.*⁸⁴ reported values of $\Delta_{Tet.}$ between 2.20 and
 11 2.26 Å, a tilt angle (γ_{tilt}) between 6.6 and 7.8°, and a rotation angle of tetrahedra ($\alpha_{rot.}$)
 12 equal to 11°. By simulation, as we observed on the neutral clay,⁴⁷ the PIM force field
 13 predicts values of $\Delta_{Tet.}$, γ_{tilt} and $\alpha_{rot.}$ in good agreement with experimental ones while
 14 the ClayFF force field underestimates these properties. The experimental shape of the
 15 cavities is ditrigonal.^{57,72,84–86} It is well reproduced with the PIM force field whereas with
 16 the non-polarizable one we obtain hexagonal cavities. These different results are illustrated
 17 in Figure 8. This success of the PIM force field is permitted by its better account of the
 18 flexibility of the structure. The flexibility also has a crucial impact on the local structure
 19 and properties of the interlayer species at the surface of the layer, for example the position
 20 of the cations beside the hexagonal cavities.

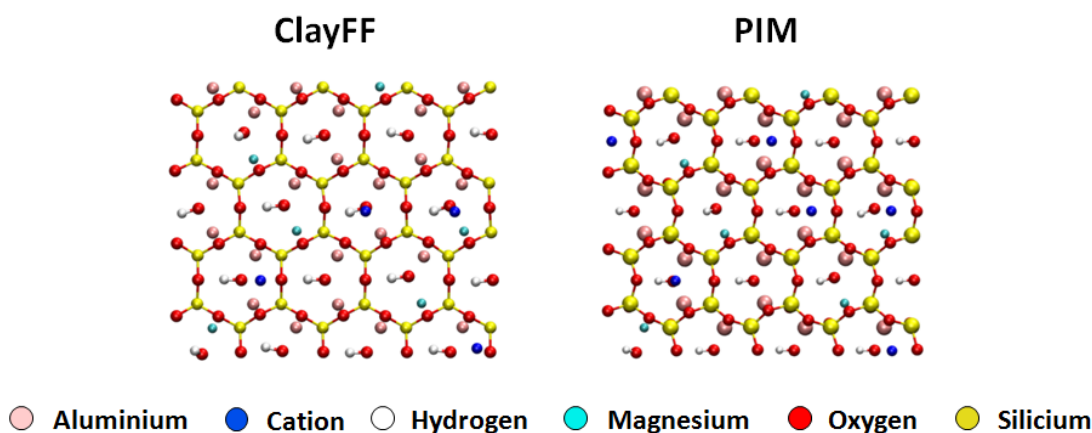
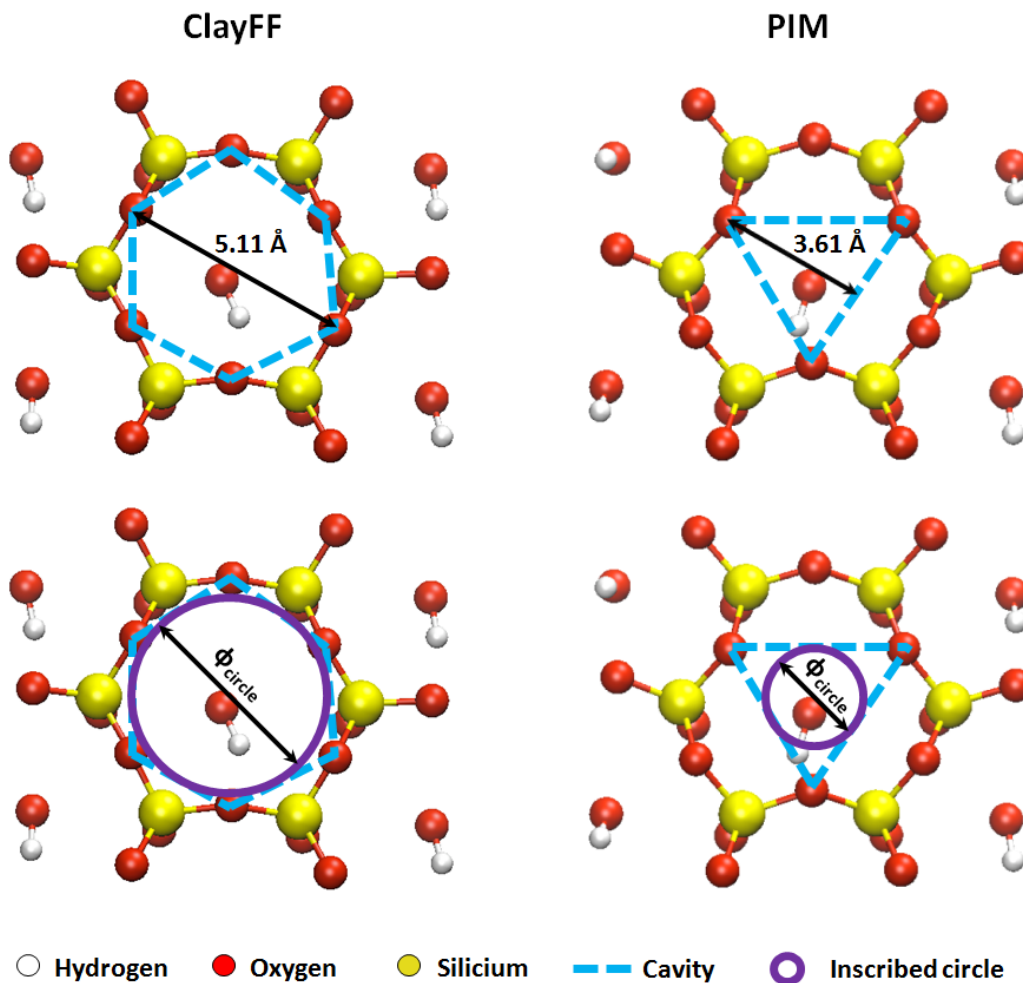


Figure 8: Ring arrangements of montmorillonites obtain with the ClayFF et the PIM force field.

Cation adsorption

As we previously mentioned, the interlayer distance h is underestimated with the ClayFF force field, whereas it is quite well reproduced with the PIM force field. These differences can now be explained by the shape and dimensions of the cavities and the cations size. Indeed, the shape of the cavities is hexagonal with ClayFF and ditrigoal with PIM. In the hexagonal cavities formed by six basal oxygens, the distance between two opposite basal oxygens is equal to 5.11(8) Å and the diameter of the inscribed circle (Φ_{circle} in Figure 9) to 4.42(8) Å. The specific shape of ditrigoal cavities results in a smaller space limited by three basal oxygens pointing to the center. The height of this triangular cavity is 3.61(7) Å and the diameter of the inscribed circle is only 2.41(7) Å. These different sizes of cavities are shown in Figure 9. The cation is located in the center of the inscribed circle (Figure 10). Depending on the shape of the cavity, the interlayer ion may enter more or less deeply (Figure 10). The radii⁸⁷ of the considered ions are equal to 1.02 Å (Na^+), 1.00 Å (Ca^{2+}), 1.16 Å (Sr^{2+}) and 1.70 Å (Cs^+). The sodium, calcium and strontium cations may enter easily into the hexagonal cavities, whereas in the case of the ditrigoal cavities they are positioned just above. Because cesium is too large, it remains above the cavities in both cases: the results obtained with both force fields are therefore similar for this cation (see Supplementary Figure S2). For all systems, the larger the size of the cation ($\text{Na}^+ < \text{Ca}^{2+} < \text{Sr}^{2+} < \text{Cs}^+$) the farther it is from surface. The wider hexagonal cavities predicted by ClayFF can accommodate all cations except for the larger cesium. In contrast, the PIM force field predicts that all ions reside above the narrower di-trigoal cavities, at an increasing distance from the tetrahedral sheet with increasing ionic radius (see Figures S2 and S3). Overall, we can conclude that the better agreement with experiments for the interlayer distance h obtained with PIM compared to ClayFF is due to the better description of the adsorption of the cations inside the cavities, which in turn is permitted by the better account of the framework flexibility. We now investigate the transferability of the PIM to other aluminosilicates, namely zeolites.



36
37
38
39

Figure 9: Form and size of the hexagonal and ditrignal cavity. The blue dotted lines represent the periphery of the cavity.

40 41 42 43 44 45 46 47 48 49 50 51 52 53 54 55

Transferability to Zeolites

46
47
48
49
50
51
52
53
54
55

Unlike two-dimensional phyllosilicates such as clays, zeolites display a three-dimensional framework, consisting only of tetrahedral units, with a diversity of topologies for their assembly.⁴ Substitutions of Si^{4+} by Al^{3+} ions result as for clays in a negative charge compensated by counterions. Multivalent counterions may deform locally the mineral framework and such deformation impacts the distribution of the cations among the crystallographic sites where they can reside.

56
57
58
59
60

Zeolites therefore provide a stringent test on the ability of the PIM force field to correctly

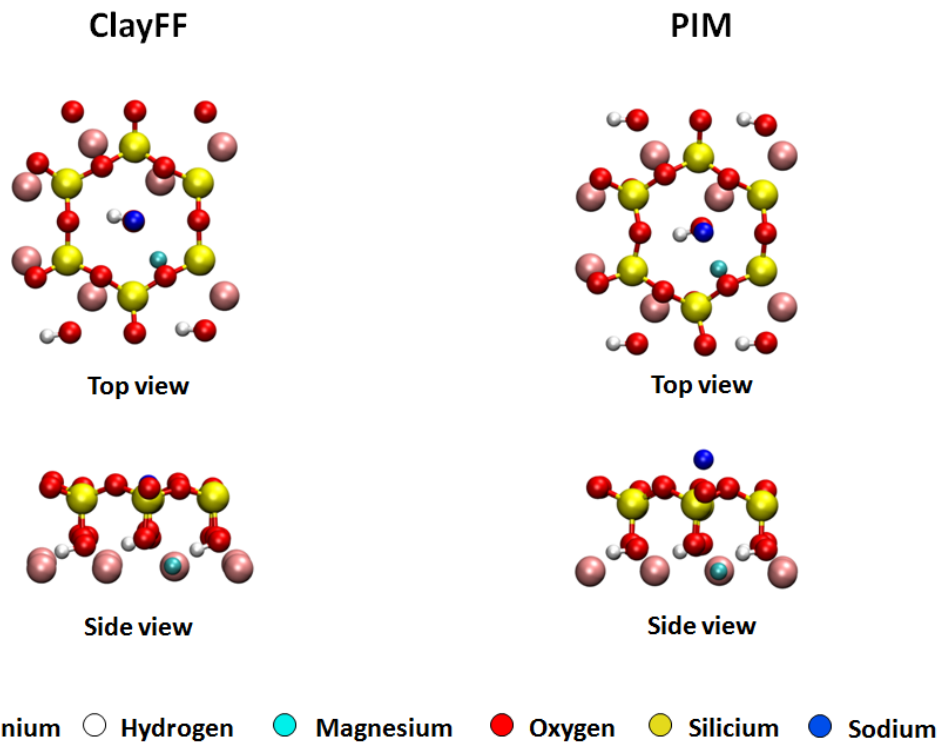


Figure 10: Top and side view of the position of the Na cation above the cavity.

describe i) the three-dimensional framework, which displays a more open structure than clay layers and ii) its local deformation by multivalent counterions. It is important to keep in mind, beyond the issue of transferability of the PIM, that there is a need for classical force fields able to accurately describe the flexibility of the framework,⁸⁸ since standard force fields typically consider the latter as rigid.^{21,89–94} This further implies the knowledge of the structure from prior experiments. Specifically, we consider here faujasite (FAU) which is the most widely studied zeolite type.⁴ Their crystal structure and the corresponding cationic sites are well known, even though their precise position and occupancy can differ depending on the cations nature and content.⁵

Simulation Details

The cubic simulation box contains one unit cell (space group Fd3m) of composition $M_{x/n}Si_{192-x}Al_xO_{384}$ (see Figure 11), where M^{n+} refers to sodium (Na^+), calcium (Ca^{2+}), or strontium (Sr^{2+}).

We consider here two different zeolites, Y-faujasite with a Si/Al ratio of 2.3 ($x = 58$) and X-faujasite with a Si/Al of 1 ($x = 96$). The distribution of substitutions complies with Loewenstein's rule (-Al-O-Al- sequences are prohibited), so that they are alternated in the latter case, but is otherwise random in the former case since it was shown that there is no preferential organization in Y-faujasite.⁹⁵

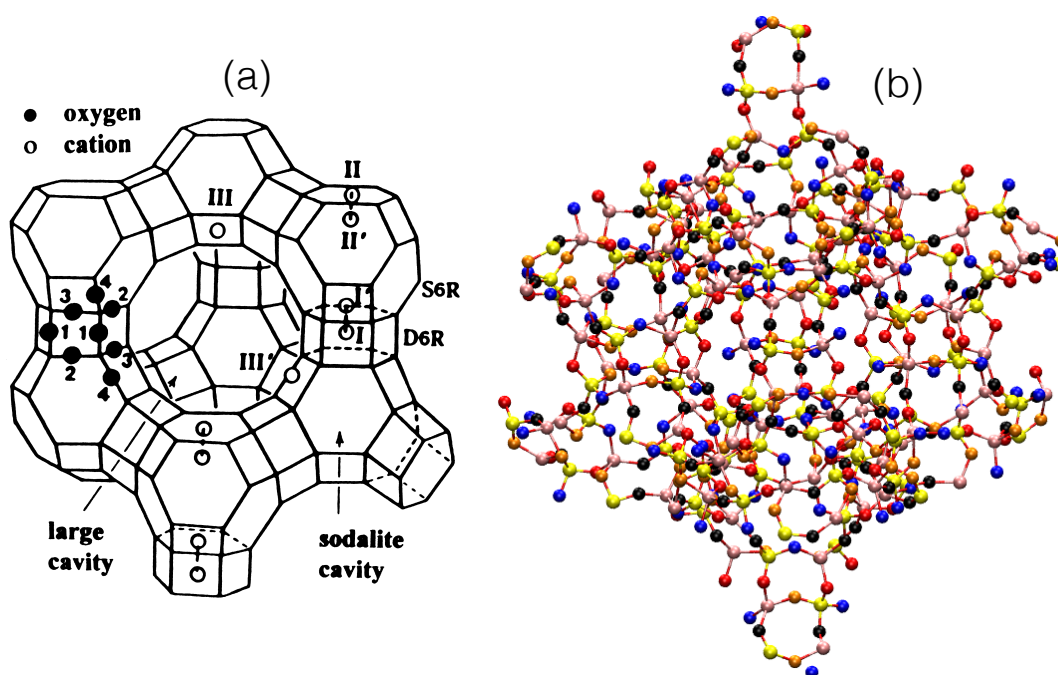


Figure 11: (a) Framework structure of faujasite zeolites.⁹⁶ There are 4 nonequivalent oxygen atom types, labelled from 1 to 4 (see text). Extraframework cationic sites are labelled I, I', II, II' and III. (b) Snapshot of faujasite structure used for molecular simulations.

Molecular dynamics simulations with the PIM force field are performed using the CP2K package. After a preliminary test, it was found that the parameters describing the interaction of Al^{3+} in octahedral units, as obtained in the previous section for clays, were not able to stabilize the zeolite structure in which Al^{3+} experiences a tetrahedral environment. For a direct transferability, it would have been necessary to also include such a case (substitutions in the tetrahedral sheet). Rather, here we simply use for aluminum the same parameters as

1
2
3 for silicon, except of course for the formal charge. As we now proceed to show, this ansatz,
4 physically motivated by the fact that both ions are isoelectronic, is sufficient to achieve our
5 goals.
6
7
8

9
10 In order to properly sample all relevant configurations of counterions at 300 K, which
11 are separated by much larger energy barriers than in the case of clays, we use the simulated
12 annealing method.^{97,98} The cations move significantly away from their initial configurations
13 only at very high temperature. In practice, we perform simulations at 2000 K. However, at
14 such a temperature the framework is not stable, at least as described by the PIM. Therefore,
15 during simulations at 2000 K the framework is kept rigid (NVT simulation, during 50 ps).
16 Then, the structure is relaxed at a temperature of only 700 K (NPT ensemble at a pressure
17 of 1 bar, during 50 ps). The temperature is then brought back to 300 K where equilibrium
18 properties are sampled, before starting a new annealing cycle (to check the convergence of
19 the cation distribution). The thermostat and barostat time constants are respectively equal
20 to 1 ps and 5 ps.
21
22
23
24
25
26
27
28
29
30
31

32 The extraframework cations may be found in various sites, indicated in Figure 11. In
33 order to assign a given cation to a type of site (I, I', II, II' or III, see below), we use a new
34 method that we introduced recently.⁸⁹ Contrary to standard approaches, which requires the
35 knowledge of the precise location of the crystallographic sites from experiments, this method
36 also applies to the case of flexible structures, as it is based on the local environment of the
37 cation (coordination by the different types of oxygen atoms, see Figure 11a).
38
39
40
41
42
43
44
45

46 Framework Structure

47
48 The faujasite structure contains three distinct types of cages which are known as supercages,
49 sodalites, and hexagonal prisms (Figure 11). Four distinct oxygen atoms can be found
50 in faujasite. O1 bridging oxygens form the edges of the lateral faces of hexagonal prisms.
51 O2 and O3 are alternatively found along the edges of the hexagonal faces of these prisms,
52 which connect them to the neighbouring cuboctahedral sodalite cages. More precisely, O3
53
54
55
56
57
58
59
60

1
2
3 belong to the square faces of the sodalite cages, while O2 belong to the hexagonal windows
4 between the sodalite and supercages. Lastly, O4 oxygen atoms are located on the shared
5 edges between the square faces and sodalite-supercage hexagonal windows.
6
7
8

9
10 As a first test of the performance of the PIM model, we analyze the structure of the
11 mineral framework. More precisely, Tables 8 and 9 report the average TO distances (with
12 T=Al or Si) and TOT angles for the various oxygen types, as well as the lattice parameter,
13 for Y and X faujasite, respectively. In each table, the simulation results are compared with
14 experimental data, when available.^{7,89,99–101}
15
16
17
18

19 The lattice parameter is in good agreement with experiments, within $\sim 2\%$ for both
20 Si/Al ratios and all counterions. In addition, the PIM force field is able to capture the
21 lattice contraction with increasing Si/Al ratio (from X to Y). In NaY, all angles and distances
22 are approximately equal ($\sim 140^\circ$ and $\sim 1.7 \text{ \AA}$, respectively) and in good agreement with
23 experiments. The bond lengths are slightly shorter, in CaY and SrY compared to NaY.
24 In addition, the tetrahedra are now distorted, with different TOT angles depending on the
25 considered oxygen type. In particular, the TO(1)T, TO(2)T and TO(3)T angles decrease,
26 while the TO(4)T angle slightly increases from NaY to Ca/SrY, in line with the experimental
27 results. This local deformation of the structure may be at the origin of the larger standard
28 deviation on the bond lengths (compared to NaY), as well as of the 1-2 % difference in the
29 lattice parameter with respect to experiments. Consistently with the evolution of the lattice
30 parameter with Si/Al ratio, one observes a slight shortening of the TO bond lengths from
31 CaX to CaY and from SrX to SrY. Overall, the PIM model which was not parametrized on
32 zeolites is able to correctly describe the structure of the faujasite framework, including its
33 evolution with Si/Al ratio (at least in the considered range, *i.e.* 1-2.3) and its deformation
34 induced by divalent cations. This is in itself a significant achievement of the present PIM.
35
36
37
38
39
40
41
42
43
44
45
46
47
48
49
50
51
52
53
54
55
56
57
58
59
60

1
2
3
4
5
6
7
8
9
10
11
12
13
14
15
16
17
18
19
20
21
22
23
24
25
26
27
28
29
30
31
32
33
34
35
36
37
38
39
40
41
42
43
44
45
46
47
48
49
50
51
52
53
54
55
56
57
58
59
60

Method	Angles ($^{\circ}$)				Distances (\AA)				Lattice parameter (\AA)	
	TO(1)T	TO(2)T	TO(3)T	TO(4)T	TO(1)	TO(2)	TO(3)	TO(4)		
	NaY									
Sim.	137.1 ± 0.7	137.5 ± 0.7	136.0 ± 0.8	137.5 ± 0.6	1.69 ± 0.05	1.73 ± 0.1	1.73 ± 0.1	1.73 ± 0.1	24.4 ± 0.1	
Exp. ⁷	137.9	145.0	140.5	146.9	1.63	1.65	1.67	1.65	24.85 ± 0.03	
Exp. ¹⁰²	150	156	141	138	1.63	1.63	1.70	1.58	24.71 ± 0.02	
	CaY									
Sim.	124.2 ± 0.7	131.2 ± 0.5	124.4 ± 0.7	142.2 ± 0.8	1.66 ± 0.15	1.68 ± 0.14	1.70 ± 0.10	1.65 ± 0.1	24.2 ± 0.1	
Exp. ¹⁰³	-	-	-	-	1.63	1.65	1.67	1.62	24.71	
	SrY									
Sim.	123.3 ± 2.1	132.1 ± 1.1	126.3 ± 2.2	142.4 ± 1.9	1.66 ± 0.15	1.68 ± 0.14	1.71 ± 0.18	1.65 ± 0.1	24.2 ± 0.12	
Exp. ¹⁰⁴	129	152	146	165	1.65	1.64	1.67	1.60	24.84	

Table 8: Interatomic angles and distances, and lattice parameter for dehydrated Y-faujasite zeolites. Simulation results with the PIM force field are compared with experimental data, when available.

Method	Angles ($^{\circ}$)				Distances (\AA)				Lattice parameter (\AA)	
	TO(1)T	TO(2)T	TO(3)T	TO(4)T	TO(1)	TO(2)	TO(3)	TO(4)		
	CaX									
Sim.	117.0 ± 1.7	124.9 ± 0.8	120.7 ± 2.0	143.2 ± 1.8	1.67 ± 0.05	1.73 ± 0.09	1.75 ± 0.14	1.69 ± 0.09	24.60 ± 0.03	
Exp. ¹⁰⁵	130.4	141.4	131.6	164.3	1.63	1.6	1.65	1.55	25.10	
Exp. ¹⁰⁶	125.9	140.8	130.2	169.2	1.66	1.69	1.7	1.66	25.00	
	SrX									
Sim.	119.1 ± 2.3	127.0 ± 1.0	122.8 ± 1.5	140.3 ± 2.2	1.67 ± 0.07	1.73 ± 0.12	1.74 ± 0.12	1.69 ± 0.09	24.70 ± 0.1	
Exp. ¹⁰⁷	126.7	150.8	137.7	160.3	1.66	1.68	1.69	1.66	25.21	

Table 9: Interatomic angles and distances, and lattice parameter for dehydrated X-faujasite zeolites. Simulation results with the PIM force field are compared with experimental data, when available.

1
2
3
4
5
6
7
8
9
10
11
12
13
14
15
16
17
18
19
20
21
22
23
24
25
26
27
28
29
30
31
32
33
34
35
36
37
38
39
40
41
42
43
44
45
46
47
48
49
50
51
52
53
54
55
56
57
58
59
60

Distribution of Extraframework Cations

Another key feature of zeolites, particularly important for their applications, is the distribution of the extraframework cations among the various sites illustrated in Figure 11a: Site I is at the center of the hexagonal prism; site I' is the image of site I in the sodalite cage; site II' is also inside the sodalite cage, near the center of hexagonal windows; site II is the image of site II' inside the supercage; finally, site III/III' is inside the supercage at/near the center of the four-ring placed between two other four-rings.

The results obtained with the PIM force field are reported in Tables 10 and 11 for Y and X-faujasites, respectively. These tables also report corresponding experimental data, when available. As can be seen in both tables, the results of the simulations with the PIM model are in excellent agreement with the experimental results for the cation distribution. In NaY almost all sites II (32 sites per unit cell) are occupied by Na^+ cations, while sites II' and III/III' are generally empty. The remaining cations occupy sites I and I'. In Ca- and Sr-exchanged Y and X-faujasites, the more confined sites I (and I') are occupied preferentially (16 hexagonal prisms), while the remaining cations reside in sites II.

Finally, we note that in the dry states considered in the present study, the cationic distribution is dominated by interionic repulsion. A more stringent test of the performance of the PIM force field would be the case of hydrated zeolites, which would require the parametrization of the water-aluminosilicate interaction. We therefore leave this for further investigation. A recent study of cation migration upon (de)hydration in partially Ni-exchanged Na-faujasite⁹⁰ demonstrated the importance of accounting for the framework deformation to properly predict the distribution of cations among the various sites and its evolution with water content. Even though the purpose of the present work was to demonstrate the transferability of the PIM force field, the results are also promising for future studies dedicated to zeolites.

Method	Composition	Distribution of cations						N_{total}^{cation}
		I	I'	II	II'	III/III'	not localized	
		NaY						
Sim.	$\text{Na}_{58}\text{Si}_{134}\text{Al}_{58}\text{O}_{384}\text{Y}$	8.9 ± 0.9	18.0 ± 1.3	30.2 ± 1.0	–	0.7 ± 0.4	0.1 ± 0.3	57.7
Exp. ¹⁰⁸	$\text{Na}_{58}\text{Si}_{134}\text{Al}_{58}\text{O}_{384}\text{Y}$	9.3	16.7	31.3	–	–	–	57.3
Exp. ¹⁰²	$\text{Na}_{57}\text{Si}_{135}\text{Al}_{57}\text{O}_{384}\text{Y}$	8.0	18.9	30.1	–	–	–	57
		CaY						
Sim.	$\text{Ca}_{29}\text{Si}_{134}\text{Al}_{58}\text{O}_{384}\text{Y}$	14.4 ± 1.0	2.2 ± 1.0	9.9 ± 0.6	–	0.5	1.9 ± 0.2	27.1
Exp. ¹⁰³	$\text{Ca}_{27}\text{Si}_{133}\text{Al}_{57}\text{O}_{384}\text{Y}$	14.2 ± 0.3	2.6 ± 0.4	11.4 ± 0.4	–	–	–	28.2
Exp. ¹⁰⁹	$\text{Ca}_{26.8}\text{Na}_{3.4}\text{Si}_{135}\text{Al}_{56.9}\text{O}_{384}\text{Y}$	15.4 ± 0.8	–	12.8 ± 1.3	–	–	–	28.2
		SrY						
Sim.	$\text{Sr}_{29}\text{Si}_{134}\text{Al}_{58}\text{O}_{384}\text{Y}$	14.5 ± 0.9	1.9 ± 0.2	10.9 ± 0.8	–	0.5	1.1 ± 0.2	27.9
Exp. ¹⁰⁴	$\text{Sr}_{24.5}\text{Na}_{3.4}\text{K}_{3.1}\text{Si}_{136.5}\text{Al}_{55.5}\text{O}_{384}\text{Y}$	$10.9 - 12.8$	$2.6 - 6.4$	$9.6 - 11.2$	–	–	–	–

Table 10: Distribution of cations between the various sites (number of cations per unit cell) for dehydrated Y-faujasite. Simulation results with the PIM force field are compared with experimental data, when available.

1
2
3
4
5
6
7
8
9
10
11
12
13
14
15
16
17
18
19
20
21
22
23
24
25
26
27
28
29
30
31
32
33
34
35
36
37
38
39
40
41
42
43
44
45
46
47
48
49
50
51
52
53
54
55
56
57
58
59
60

Method	Composition	Distribution of cations						N_{total}^{cation}
		I	I'	II	II'	III/III'	not localized	
CaX								
Sim.	$Ca_{48}Si_{96}Al_{96}O_{384}X$	14.9 ± 0.6	0.9 ± 0.2	30.1 ± 0.7	–	0.5	2.1 ± 0.7	45.9
Exp. ¹⁰⁵	$Ca_{48}Si_{96}Al_{96}O_{384}X$	11.9	5	31.1	–	–	–	48
Exp. ¹⁰⁶	$Ca_{46}Si_{100}Al_{92}O_{384}X$	16.2	–	29.4	–	–	–	45.6
Exp. ¹¹⁰	$Ca_{46}Si_{100}Al_{92}O_{384}X$	16.7	–	30.2	–	–	–	46.9
Exp. ¹¹⁰	$Ca_{46}Si_{100}Al_{92}O_{384}X$	16.3	–	31.3	–	–	–	47.6
SrX								
Sim.	$Sr_{48}Si_{96}Al_{96}O_{384}X$	16.2 ± 0.5	0.5 ± 0.1	27.7 ± 0.9	0.4 ± 0.2	–	3.2 ± 0.9	44.8
Exp. ¹⁰⁷	$Sr_{46}Si_{100}Al_{92}O_{384}X$	16.2	–	29.2	–	–	–	45.4

Table 11: Distribution of cations between the various sites (number of cations per unit cell) for dehydrated Y-faujasite. Simulation results with the PIM force field are compared with experimental data, when available.

1
2
3
4
5
6
7
8
9
10
11
12
13
14
15
16
17
18
19
20
21
22
23
24
25
26
27
28
29
30
31
32
33
34
35
36
37
38
39
40
41
42
43
44
45
46
47
48
49
50
51
52
53
54
55
56
57
58
59
60

Conclusion

We have successfully extended the PIM polarizable force field to montmorillonites. We used exactly the same procedure as for neutral clays⁴⁷ in order to obtain the force field parameters. The PIM force field was built and validated for two charged clays: *tv*- and *cv*-montmorillonites with four different cations (Na^+ , Ca^{2+} , Sr^{2+} and Cs^+). A structural description of the atomic clay structure is obtained with the new polarizable ion model (PIM) and compared, together with the state-of-the-art non-polarizable force field for clays (ClayFF), to experimental data. The global structure of the unit cell is well reproduced by both force fields. However, introducing the polarization allows for a better description of the structural flexibility and the physisorption of cations at the tetrahedral sheet surface.

Moreover, we have demonstrated the transferability of the PIM model for other aluminosilicates, at the price of a slight adjustment of the force field, namely using the Si-O short range interactions for tetrahedral Al, instead of the parameters determined for octahedral Al in montmorillonite clay. To this end, we considered the most widely studied zeolites, of faujasite-type. Specifically, we investigated NaY and completely exchanged X and Y faujasites with Ca^{2+} and Sr^{2+} cations. A good agreement with experiments was obtained for the mineral framework structure, including the variations with Si/Al ratio and change in extraframework cation, which is already an achievement in itself. Furthermore, the predicted distribution of extraframework cations is also in excellent agreement with experiments.

The next step in the development of the polarizable force field consists in extending the present approach to hydrated Na-, Cs-, Ca- and Sr-montmorillonites. The PIM force field should then provide a more accurate description of liquid-solid interfaces in such systems. In turn, this will improve our understanding of the interaction of clay minerals with water, including swelling and wettability. Moreover, owing the good performance of the PIM force field for dry Faujasite-type zeolites, we can expect that the parametrization of water-mineral interactions will allow the full study of the simultaneous migration of the cations and the deformation of the framework upon hydration. This approach could also be extended to

1
2
3 other aluminosilicates and multivalent ions of industrial and environmental interest (f-block
4 elements, rare Earths, etc.).
5
6
7
8

9 10 **Supporting Information Available**

11
12
13 Parameters of the PIM force field obtained on pyrophyllite and talc, Trans- and Cis-vacant
14 Na-, Ca-, Sr- and Cs-montmorillonite sheets structures details, Cations adsorption on the
15 tetrahedral sheet surface, and the parameters of the ClayFF force field.
16
17
18

19 This material is available free of charge via the Internet at <http://pubs.acs.org/>.
20
21
22

23 **Acknowledgement**

24
25
26
27 S.T. acknowledges financial support from Labex MiChem, W.L. from Région Ile-de-France
28 via the DIM OXYMORE and V.M. from NEEDS-MIPOR via project TRANSREAC. We
29 also thank the Direction des Systèmes d'Information of Jussieu for access to computational
30 resources. We are grateful for the computing resources on OCCIGEN (CINES, French Na-
31 tional HPC) obtained through the projects x2015097321 and x2016087684.
32
33
34
35
36
37
38
39
40
41
42
43
44
45
46
47
48
49
50
51
52
53
54
55
56
57
58
59
60

References

- (1) Ricq, M. La classification des minéraux argileux (phyllosilicates). *Rev. Geo. Alp.* **1965**, *53*, 708–711.
- (2) Wentworth, C. K. A scale of grade and class terms for clastic sediments. *J. Geol.* **1922**, *30*, 377–392.
- (3) Nickel-Strunz Classification - Primary Groups 10th edition. <http://www.mindat.org/strunz.php>, (accessed November 19, 2016).
- (4) Database of zeolite structures. <http://www.iza-structure.org/databases/>, (accessed November 19, 2016).
- (5) Mortier, W. J. *Compilation of extra framework sites in zeolites*; Butterworth & Co. Ltd, 1982.
- (6) Radoslovich, E. W.; Norrish, K. Cell dimensions and symmetry of layer-lattice silicates. I. Some structural considerations. *Am. Mineral.* **1962**, *47*, 599.
- (7) Fitch, A. N.; Jovic, H.; Renouprez, A. Localization of benzene in sodium-y-zeolite by powder neutron diffraction. *J. Phys. Chem.* **1986**, *90*, 1311–1318.
- (8) Brandani, F.; Ruthven, D. M. The effect of water on the adsorption of CO₂ and C₃H₈ on type x-zeolites. *Eng. Chem. Res.* **2004**, *43*, 8339–8344.
- (9) Pitteloud, C.; Powell, D. H.; Soper, A. K.; Benmore, C. J. The structure of inter-layer water in wyoming montmorillonite studied by neutron diffraction with isotopic substitution. *Physica B* **2000**, *276*, 236–237.
- (10) Rinnert, E.; Carteret, C.; Humbert, B.; Fragneto-Cusani, G.; Ramsay, J. D. F.; Delville, A.; Robert, J.-L.; Bihannic, I.; Pelletier, M.; Michot, L. J. Hydration of a synthetic clay with tetrahedral charges: A multidisciplinary experimental and numerical study. *J. Phys. Chem. B* **2005**, *109*, 23745–23759.

- 1
2
3
4 (11) Ferrage, E.; Lanson, B.; Sakharov, B. A.; Geoffroy, N.; Jacquot, E.; Drits, V. A. Investigation of dioctahedral smectite hydration properties by modeling of x-ray diffraction
5
6
7
8
9
10
11
12
13
14
15
16
17
18
19
20
21
22
23
24
25
26
27
28
29
30
31
32
33
34
35
36
37
38
39
40
41
42
43
44
45
46
47
48
49
50
51
52
53
54
55
56
57
58
59
60
- (12) Angela, D. L. Méthodes de simulation moléculaire pour l'étude de la distribution des cations et de l'adsorption de molécules polaires dans les zéolithes. Ph.D. Dissertation, Université d'Orsay - Paris XI, 2007.
- (13) Kalinichev, A. G.; Wang, J.; Kirkpatrick, R. J. Molecular dynamics modeling of the structure, dynamics and energetics of mineral-water interfaces: Application to cement materials. *Cem. Concr. Res.* **2007**, *37*, 337–347.
- (14) Berghout, A.; Tunega, D.; Zaoui, A. Density functional theory (DFT) study of the hydration steps of $\text{Na}^+/\text{Mg}^{2+}/\text{Ca}^{2+}/\text{Sr}^{2+}/\text{Ba}^{2+}$ exchanged montmorillonites. *Clays Clay Miner.* **2010**, *58*, 174–187.
- (15) Jeffroy, M. Molecular simulation of cationic zeolites properties: Thermodynamic and structural properties. Ph.D. Dissertation, Université Paris Sud - Paris XI, 2010.
- (16) Combariza, A. F.; Gomez, D. A.; Sastre, G. Simulating the properties of small pore silicazeolites using interatomic potentials. *Chem. Soc. Rev.* **2013**, *42*, 114–127.
- (17) Katti, D. R.; Upadhyay, H. B.; Katti, K. S. Molecular interactions of kerogen moieties with na-montmorillonite: An experimental and modeling study. *Fuel* **2014**, *130*, 34–45.
- (18) Hirasaki, G. J. Wettability: Fundamentals and surface forces. *SPE Form. Eval.* **1991**, *6*, 217–226.
- (19) Fuchs, A. H.; Cheetham, A. K. Adsorption of guest molecules in zeolitic materials: Computational aspects. *J. Phys. Chem. B* **2001**, *105*, 7375–7383.

- 1
2
3
4
5
6
7
8
9
10
11
12
13
14
15
16
17
18
19
20
21
22
23
24
25
26
27
28
29
30
31
32
33
34
35
36
37
38
39
40
41
42
43
44
45
46
47
48
49
50
51
52
53
54
55
56
57
58
59
60
- (20) Boddenberg, B.; Rakhmatkariev, G. U.; Hufnagel, S.; Salimov, Z. A calorimetric and statistical mechanics study of water adsorption in zeolite NaY. *Phys. Chem. Chem. Phys.* **2002**, *4*, 4172–4180.
- (21) Jeffroy, M.; Borissenko, E.; Boutin, A.; Di Lella, A.; Porcher, F.; Souhassou, M.; Lecomte, C.; Fuchs, A. H. Evidence of a framework induced cation redistribution upon water adsorption in cobalt exchanged x faujasite zeolite: A joint experimental and simulation study. *Microporous Mesoporous Mater.* **2011**, *138*, 45–50.
- (22) Solc, R.; Gerzabek, M. H.; Lischka, H.; Tunega, D. Wettability of kaolinite (001) surfaces - molecular dynamic study. *Geoderma* **2011**, *169*, 47–54.
- (23) Sethia, G.; Somani, R. S.; Chand Bajaj, H. Adsorption of carbon monoxide, methane and nitrogen on alkaline earth metal ion exchanged zeolite-x: Structure, cation position and adsorption relationship. *RSC Adv.* **2015**, *5*, 12773–12781.
- (24) Du, H.; Miller, J. D. A molecular dynamics simulation study of water structure and adsorption states at talc surfaces. *Int. J. Miner. Process.* **2007**, *84*, 172–184.
- (25) Marry, V.; Rotenberg, B.; Turq, P. Structure and dynamics of water at a clay surface from molecular dynamics simulation. *Phys. Chem. Chem. Phys.* **2008**, *10*, 4802–4813.
- (26) Rotenberg, B.; Patel, A. J.; Chandler, D. Molecular explanation for why talc surfaces can be both hydrophilic and hydrophobic. *J. Am. Chem. Soc.* **2011**, *133*, 20521–20527.
- (27) Pitman, M. C.; van Duin, A. C. T. Dynamics of confined reactive water in smectite clay-zeolite composites. *J. Am. Chem. Soc.* **2012**, *134*, 3042–3053.
- (28) Whitley, H. D.; Smith, D. E. Free energy, energy, and entropy of swelling in cs-, na-, and sr-montmorillonite clays. *J. Chem. Phys.* **2004**, *120*, 5387–5395.
- (29) Tambach, T. J.; Bolhuis, P. G.; Hensen, E. J. M.; Smit, B. Hysteresis in clay swelling

- 1
2
3 induced by hydrogen bonding: Accurate prediction of swelling states. *Langmuir* **2006**,
4 *22*, 1223–1234.
5
6
7
- 8 (30) McGrath, M. J.; Siepmann, J. I.; Kuo, I.-F. W.; Mundy, C. J.; VandeVondele, J.;
9 Hutter, J.; Mohamed, F.; Krack, M. Simulating fluid-phase equilibria of water from
10 first principle. *J. Phys. Chem. A* **2006**, *110*, 640–646.
11
12
13
- 14 (31) Loganathan, N.; Yazaydin, A. O.; Bowers, G. M.; Kalinichev, A. G.; Kirkpatrick, R. J.
15 Structure, energetics and dynamics of Cs⁺ and H₂O in hectorite: Molecular dynamics
16 simulations with an unconstrained substrate surface. *J. Phys. Chem. C* **2016**, *120*,
17 10298–10310.
18
19
20
21
22
23
- 24 (32) Malikova, N.; Marry, V.; Dufrêche, J.-F.; Simon, C.; Turq, P.; Giffaut, E. Temperature
25 effect in a montmorillonite clay at low hydration - microscopic simulation. *Mol. Phys.*
26 **2004**, *102*, 1965–1977.
27
28
29
30
- 31 (33) Padma Kumar, P.; Kalinichev, A. G.; Kirkpatrick, R. J. Hydration, swelling, interlayer
32 structure, and hydrogen bonding in organolayered double hydroxides: Insights from
33 molecular dynamics simulation of citrate-intercalated hydrotalcite. *J. Phys. Chem. B*
34 **2006**, *110*, 3841–3844.
35
36
37
38
39
- 40 (34) Malikova, N.; Cadène, A.; Marry, V.; Dubois, E.; Turq, P. Diffusion of water in clays
41 on the microscopic scale: Modeling and experiment. *J. Phys. Chem. B* **2006**, *110*,
42 3206–3214.
43
44
45
46
- 47 (35) Greathouse, J. A.; Cygan, R. T. Molecular dynamics simulation of uranyl(vi) adsorp-
48 tion equilibria onto an external montmorillonite surface. *Phys. Chem. Chem. Phys.*
49 **2005**, *7*, 3580–3586.
50
51
52
53
- 54 (36) Greathouse, J. A.; Cygan, R. T. Water structure and aqueous Uranyl(vi) adsorp-
55 tion equilibria onto external surfaces of beidellite, montmorillonite, and pyrophyllite:
56 Results from molecular simulations. *Environ. Sci. Technol.* **2006**, *40*, 3865–3871.
57
58
59
60

- 1
2
3
4
5
6
7
8
9
10
11
12
13
14
15
16
17
18
19
20
21
22
23
24
25
26
27
28
29
30
31
32
33
34
35
36
37
38
39
40
41
42
43
44
45
46
47
48
49
50
51
52
53
54
55
56
57
58
59
60
- (37) Delville, A. Structure and properties of confined liquids: A molecular model of the clay-water interface. *J. Phys. Chem.* **1993**, *97*, 9703–9712.
- (38) Marry, V.; Turq, P. Microscopic simulations of interlayer structure and dynamics in bihydrated heteroionic montmorillonites. *J. Phys. Chem. B* **2003**, *107*, 1832–1839.
- (39) Wang, J.; Kalinichev, A. G.; Kirkpatrick, R. J. Effects of substrate structure and composition on the structure, dynamics, and energetics of water at mineral surfaces: A molecular dynamics modeling study. *Geochim. Cosmochim. Ac.* **2006**, *70*, 562–582.
- (40) Boğan, A.; Marry, V.; Rotenberg, B.; Turq, P.; Noetinger, B. How electrostatics influences hydrodynamic boundary conditions: Poiseuille and electro-osmotic flows in clay nanopores. *J. Phys. Chem. C* **2013**, *117*, 978–985.
- (41) Cygan, R. T.; Liang, J.-J.; Kalinichev, A. G. Molecular models of hydroxide, oxyhydroxide, and clay phases and the development of a general force field. *J. Phys. Chem. B* **2004**, *108*, 1255–1266.
- (42) Skipper, N. T.; Refson, K.; McConnell, J. D. C. Computer calculation of water-clay interactions using atomic pair potentials. *Clay Miner.* **1989**, *24*, 411–25.
- (43) Skipper, N. T.; Chang, F.-R. C.; Sposito, G. Monte Carlo simulation of interlayer molecular structure in swelling clay minerals. I: Methodology. *Clays Clay Miner.* **1995**, *43*, 285–293.
- (44) Lopes, P. E. M.; Roux, B.; MacKerell, A. D. Molecular modeling and dynamics studies with explicit inclusion of electronic polarizability: Theory and applications. *Theor. Chem. Acc.* **2009**, *124*, 11–28.
- (45) Cieplak, P.; Dupradeau, F.-Y.; Duan, Y.; Wang, J. Polarization effects in molecular mechanical force fields. *J. Phys.: Condens. Matter* **2009**, *21*, 333102.

- 1
2
3
4
5
6
7
8
9
10
11
12
13
14
15
16
17
18
19
20
21
22
23
24
25
26
27
28
29
30
31
32
33
34
35
36
37
38
39
40
41
42
43
44
45
46
47
48
49
50
51
52
53
54
55
56
57
58
59
60
- (46) Baker, C. M. Polarizable force fields for molecular dynamics simulations of biomolecules. *WIREs Comput Mol Sci* **2015**, *5*, 241–254.
- (47) Tesson, S.; Salanne, M.; Rotenberg, B.; Tazi, S.; Marry, V. A classical polarizable force field for clays: Pyrophyllite and talc. *J. Phys. Chem. C* **2016**, *120*, 3749–3758.
- (48) Fumi, F. G.; Tosi, M. P. Ionic sizes and born repulsive parameters in the nacl-type alkali halides-I: The huggins-mayer and pauling forms. *J. Phys. Chem. Solids* **1964**, *25*, 31 – 43.
- (49) Tosi, M. P.; Fumi, F. G. Ionic sizes and born repulsive parameters in the nacl-type alkali halides-II: The generalized huggins-mayer form. *J. Phys. Chem. Solids* **1964**, *25*, 45 – 52.
- (50) Wang, B.; Truhlar, D. G. Including charge penetration effects in molecular modeling. *J. Chem. Theory Comput.* **2010**, *6*, 3330–3342.
- (51) Tang, K. T.; Toennies, J. P. An improved simple model for the van der waals potential based on universal damping functions for the dispersion coefficients. *J. Chem. Phys.* **1984**, *80*, 3726–3741.
- (52) Tazi, S. Description moléculaire des ions aux interfaces argile-eau. Ph.D. Dissertation, Université Pierre et Marie Curie - Paris 6, 2012.
- (53) Silvestrelli, P. L.; Parrinello, M. Water molecule dipole in the gas and in the liquid phase. *Phys. Rev. Lett.* **1999**, *82*, 3308–3311.
- (54) Bernasconi, L.; Wilson, M.; Madden, P. A. Cation polarizability from first-principles: Sn^{2+} . *Comp. Mater. Sci.* **2001**, *22*, 94–98.
- (55) Bernasconi, L.; Madden, P. A.; Wilson, M. Ionic to molecular transition in AlCl_3 : An examination of the electronic structure. *PhysChemComm* **2002**, *5*, 1–11.

- 1
2
3
4
5
6
7
8
9
10
11
12
13
14
15
16
17
18
19
20
21
22
23
24
25
26
27
28
29
30
31
32
33
34
35
36
37
38
39
40
41
42
43
44
45
46
47
48
49
50
51
52
53
54
55
56
57
58
59
60
- (56) Souza, I.; Wilkens, T.; Martin, R. T. Polarization and localization in insulators: Generating function approach. *Phys. Rev. B* **2000**, *62*, 1666–1683.
- (57) Bérend, I.; Cases, J. M.; François, M.; Uriot, J. P.; Michot, L. J.; Masion, A.; Thomas, F. Mechanism of adsorption and desorption of water vapor by homoionic montmorillonites: 2. The Li^+ , Na^+ , K^+ , Rb^+ , and Cs^+ exchanged forms. *Clay Clay Miner.* **1995**, *43*, 324–336.
- (58) Cases, J. M.; Berend, I.; Francois, M.; Uriot, J. P.; Michot, L. J.; Thomas, F. Mechanism of adsorption and desorption of water vapor by homoionic montmorillonite. 3. The Mg^{2+} , Ca^{2+} , Sr^{2+} and Ba^{2+} exchanged forms. *Clays Clay Miner.* **1997**, *45*, 8–22.
- (59) Tazi, S.; Molina, J. J.; Rotenberg, B.; Turq, P.; Vuilleumier, R.; Salanne, M. A transferable ab initio based force field for aqueous ions. *J. Chem. Phys.* **2012**, *136*, 114507.
- (60) CP2K developers group. <http://cp2k.berlios.de>, (accessed November 19, 2016).
- (61) Martyna, G. J.; Klein, M. L.; Tuckerman, M. Nosé-Hoover chains: The canonical ensemble via continuous dynamics. *J. Chem. Phys.* **1992**, *97*, 2635–2643.
- (62) Aguado, A.; Bernasconi, L.; Jahn, S.; Madden, P. A. Multipoles and interaction potentials in ionic materials from planewave-DFT calculations. *Faraday Discuss.* **2003**, *124*, 171–184.
- (63) Laino, T.; Hutter, J. Notes on “Ewald summation of electrostatic multipole interactions up to quadrupolar level” [J. Chem. Phys.119, 7471 (2003)]. *J. Chem. Phys.* **2008**, *129*, –.
- (64) Perdew, J. P.; Burke, K.; Ernzerhof, M. Generalized gradient approximation made simple. *Phys. Rev. Lett.* **1996**, *77*, 3865–3868.
- (65) Goedecker, S.; Teter, M.; Hutter, J. Separable dual-space gaussian pseudopotentials. *Phys. Rev. B* **1996**, *54*, 1703–1710.

- 1
2
3
4 (66) Hartwigsen, C.; Goedecker, S.; Hutter, J. Relativistic separable dual-space gaussian
5 pseudopotentials from h to rn. *Phys. Rev. B* **1998**, *58*, 3641–3662.
6
7
8 (67) Krack, M. Pseudopotentials for h to kr optimized for gradient-corrected exchange-
9 correlation functionals. *Theor. Chem. Acc.* **2005**, *114*, 145–152.
10
11
12 (68) VandeVondele, J.; Hutter, J. Gaussian basis sets for accurate calculations on molecular
13 systems in gas and condensed phases. *J. Chem. Phys.* **2007**, *127*.
14
15
16
17
18 (69) Silvestrelli, P. L. Maximally localized wannier functions for simulations with supercells
19 of general symmetry. *Phys. Rev. B* **1999**, *59*, 9703.
20
21
22
23 (70) Marzari, N.; Souza, I.; Vanderbilt, D. An introduction to maximally-localized wannier
24 functions. *Psi-K newsletter* **2003**, *57*, 129.
25
26
27
28 (71) James, F.; Roos, M. Minuit - a system for function minimization and analysis of the
29 parameter errors and correlations. *Comput. Phys. Commun.* **1975**, *10*, 343 – 367.
30
31
32
33 (72) Tsipursky, S. I.; Drits, V. A. The distribution of octahedral cations in the 2:1 layers
34 of dioctahedral smectites studied by oblique-texture electron diffraction. *Clay Miner.*
35 **1984**, *19*, 177–193.
36
37
38
39 (73) Vantelon, D.; Montarges-Pelletier, E.; Michot, L. J.; Pelletier, M.; Thomas, F.;
40 Briois, V. Iron distribution in the octahedral sheet of dioctahedral smectites. An Fe
41 k-edge x-ray absorption spectroscopy study. *Phys. Chem. Miner.* **2003**, *30*, 44–53.
42
43
44
45 (74) Martyna, G. J.; Tobias, D. J.; Klein, M. L. Constant pressure molecular dynamics
46 algorithms. *J. Chem. Phys.* **1994**, *101*, 4177–4189.
47
48
49
50 (75) Kolafa, J. Time-reversible always stable predictor–corrector method for molecular dy-
51 namics of polarizable molecules. *J. Comput. Chem.* **2004**, *25*, 335–342.
52
53
54
55 (76) Norrish, K. The swelling of montmorillonite. *Discuss. Faraday Soc.* **1954**, *18*, 120–134.
56
57
58
59
60

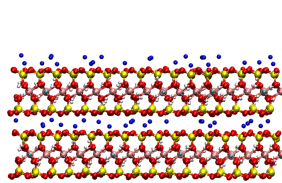
- 1
2
3
4 (77) Keren, R.; Shainberg, I. Water vapor isotherms and heat of immersion of na/ca-
5 montmorillonite systems: I, homoionic clay. *Clays Clay Miner.* **1975**, *23*, 193–200.
6
7
8
9 (78) Ferrage, E.; Lanson, B.; Malikova, N.; Plançon, A.; Sakharov, B.; Drits, V. A. New
10 insights on the distribution of interlayer water in bi-hydrated smectite from x-ray
11 diffraction profile modeling of 00l reflections. *Chem. Mater.* **2005**, *17*, 3499–3512.
12
13
14
15 (79) Ferrage, E.; Lanson, B.; Sakharov, B. A.; Drits, V. A. Investigation of smectite hy-
16 dration properties by modeling experimental x-ray diffraction patterns: Part I. Mont-
17 morillonite hydration properties. *Am. Miner.* **2005**, *90*, 1358–1374.
18
19
20
21
22 (80) Likos, W. J.; Lu, N. Pore-scale analysis of bulk volume change from crystalline inter-
23 layer swelling in Na⁺ and Ca²⁺ smectite. *Clays Clay Miner.* **2006**, *54*, 515–528.
24
25
26
27 (81) Rutherford, D. W.; Chiou, C. T.; Eberl, D. D. Effects of exchanged cation on the
28 microporosity of montmorillonite. *Clays Clay Miner.* **1997**, *45*, 534–543.
29
30
31
32 (82) Frenkel, D.; Smit, B. *Understanding molecular simulation: from algorithms to appli-*
33 *cations*, academic press ed.; Computational Science, 2002; Vol. 1.
34
35
36
37 (83) Flyvbjerg, H.; Petersen, H. G. Error estimates on averages of correlated data. *J. Chem.*
38 *Phys.* **1989**, *91*, 461–466.
39
40
41
42 (84) Drits, V. A.; McCarty, D. K.; Zviagina, B. B. Crystal-Chemical factors responsible
43 for the distribution of octahedral cations over trans- and cis-sites in dioctahedral 2:1
44 layer silicates. *Clays Clay Miner.* **2006**, *54*, 131–152.
45
46
47
48
49 (85) Beermann, T.; Brockamp, O. Structure analysis of montmorillonite crystallites by
50 convergent-beam electron diffraction. *Clay Miner.* **2005**, *40*, 1–13.
51
52
53
54 (86) Brigatti, M. F.; Galan, E.; Theng, B. K. G. *Structures and Mineralogy of Clay Min-*
55 *erals*; Handbook of Clay Science, 2006; Vol. 1.
56
57
58
59
60

- 1
2
3
4 (87) Atkins, P. W.; Jones, L. *Chimie: molécules, matière, métamorphoses*; De Boeck
5 Supérieur, 1998.
6
7
8
9 (88) Jeffroy, M.; Nieto-Draghi, C.; Boutin, A. Molecular simulation of zeolite flexibility.
10 *Mol. Simul.* **2014**, *40*, 6–15.
11
12
13 (89) Louisfrema, W.; Rotenberg, B.; Porcher, F.; Paillaud, J.-L.; Massiani, P.; Boutin, A.
14 Cation redistribution upon dehydration of Na₅₈ y faujasite zeolite: A joint neutron
15 diffraction and molecular simulation study. *Mol. Simul.* **2015**, *41*, 1371–1378.
16
17
18 (90) Louisfrema, W.; Paillaud, J.-L.; Porcher, F.; Perrin, E.; Onfroy, T.; Massiani, P.;
19 Boutin, A.; Rotenberg, B. Cation migration and structural deformations upon dehy-
20 dration of nickel-exchanged na y-zeolite: A combined neutron diffraction and monte
21 carlo study. *J. Phys. Chem. C* **2016**, *120*, 18115–18125.
22
23
24 (91) Di Lella, A.; Desbiens, N.; Boutin, A.; Demachy, I.; Ungerer, P.; Bellat, J.-P.;
25 Fuchs, A. H. Molecular simulation studies of water physisorption in zeolites. *Phys.*
26 *Chem. Chem. Phys.* **2006**, *8*, 5396.
27
28
29 (92) Abrioux, C.; Coasne, B.; Maurin, G.; Henn, F.; Boutin, A.; Di Lella, A.; Nieto-
30 Draghi, C.; Fuchs, A. H. A molecular simulation study of the distribution of cation in
31 zeolites. *Adsorption* **2008**, *14*, 743–754.
32
33
34 (93) Buttefey, S. Modélisation et simulation moléculaire des cations extra-charpentes dans
35 les zéolithes de type faujasite. Ph.D. Dissertation, Université d'Orsay - Paris XI, 2002.
36
37
38 (94) Jaramillo, E.; Auerbach, S. M. New force field for na cations in faujasite-type zeolites.
39 *J. Phys. Chem. B* **1999**, *103*, 9589–9594.
40
41
42
43 (95) Jeffroy, M.; Nieto-Draghi, C.; Boutin, A. A new molecular simulation method to
44 determine both aluminum and cation location in cationic zeolites. *Chem. Mater.* **2016**,
45 to appear (doi:10.1021/acs.chemmater.6b03011).
46
47
48
49
50
51
52
53
54
55
56
57
58
59
60

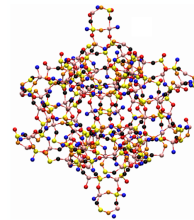
- 1
2
3
4 (96) Zhu, L.; Seff, K. Reinvestigation of the crystal structure of dehydrated sodium zeolite
5 X. *J. Phys. Chem. B* **1999**, *103*, 9512–9518.
6
7
8
9 (97) Aarts, E.; Korst, J. *Simulated annealing and boltzmann machines*; New York, NY;
10 John Wiley and Sons Inc., 1988.
11
12
13 (98) Eglese, R. W. Simulated annealing: A tool for operational research. *Eur. J. Oper. Res.*
14 **1990**, *46*, 271–281.
15
16
17
18 (99) Olson, D. H. Reinvestigation of the crystal structure of the zeolite hydrated nax. *J.*
19 *Chem. Phys.* **1970**, *74*, 2758–2764.
20
21
22
23 (100) Olson, D. H. The crystal structure of dehydrated nax. *Zeolites* **1995**, *15*, 439–443.
24
25
26 (101) Olson, D. H. Crystal structure of the zeolite nickel faujasite. *J. Phys. Chem.* **1968**,
27 *72*, 4366–4373.
28
29
30
31 (102) Eulenberger, G. R.; Shoemaker, D. P.; Keil, J. G. Crystal structures of hydrated
32 and dehydrated synthetic zeolites with faujasite aluminosilicate frameworks. I. The
33 dehydrated sodium, potassium, and silver forms. *J. Phys. Chem.* **1967**, *71*, 1812–
34 1819.
35
36
37
38
39
40 (103) Bennett, J. M.; Smith, J. V. Positions of cations and molecules in zeolites with
41 the faujasite-type framework I. Dehydrated ca-exchanged faujasite. *Mater. Res. Bull.*
42 **1968**, *3*, 633–642.
43
44
45
46
47 (104) Van Dun, J. J.; Mortier, W. J. Temperature-dependent cation distribution in zeolites.
48 1. A statistical thermodynamical model. *J. Phys. Chem.* **1988**, *92*, 6740–6746.
49
50
51
52 (105) Vitale, G.; Bull, L. M.; Morris, R. E.; Cheetham, A. K.; Toby, B. H.; Coe, C. G.;
53 MacDougall, J. E. Combined neutron and x-ray powder diffraction study of zeolite ca
54 LSX and a ^2H NMR study of its complex with benzene. *J. Phys. Chem.* **1995**, *99*,
55 16087–16092.
56
57
58
59
60

- 1
2
3
4 (106) Yeom, Y. H.; Jang, S. B.; Kim, Y.; Song, S. H.; Seff, K. Three crystal structures of
5 vacuum-dehydrated zeolite x, $M_{46}Si_{100}Al_{92}O_{384}$, $M=Mg^{2+}$, Ca^{2+} , and Ba^{2+} . *J. Phys.*
6 *Chem. B* **1997**, *101*, 6914–6920.
7
8
9
10 (107) Kim, M. J.; Jeong, M. S.; Kim, Y.; Seff, K. Crystal structures of fully dehydrated
11 fully Sr^{2+} -exchanged zeolite x and of its ammonia sorption complex. *Microporous*
12 *Mesoporous Mater.* **1999**, *30*, 233–241.
13
14
15
16
17 (108) T., H. Microfilms, University of Washington, 1972.
18
19
20 (109) Dendooven, E.; Mortier, W. J.; Uytterhoeven, J. B. Influence of temperature and
21 adsorption on the cation distribution in ca-y-zeolites. *J. Phys. Chem.* **1984**, *88*, 1916–
22 1921.
23
24
25
26
27 (110) Frising, T.; Leflaive, P. Extraframework cation distributions in x and y faujasite zeo-
28 lites: A review. *Microporous Mesoporous Mater.* **2008**, *114*, 27–63.
29
30
31
32
33
34
35
36
37
38
39
40
41
42
43
44
45
46
47
48
49
50
51
52
53
54
55
56
57
58
59
60

Polarizable Ion Model Force Field



Montmorillonite clay



Faujasite zeolite

1
2
3
4
5
6
7
8
9
10
11
12
13
14
15
16
17
18
19
20
21
22
23
24
25
26
27
28
29
30
31
32
33
34
35
36
37
38
39
40
41
42
43
44
45
46
47
48
49
50
51
52
53
54
55
56
57
58
59
60